5-2019

Spatial Reorganization of Histone-like Nucleoid Structuring Proteins Caused by Silver Nanoparticles

Meaad Alqahtany
University of Arkansas, Fayetteville

Spatial Reorganization of Histone-like Nucleoid Structuring Proteins
Caused by Silver Nanoparticles

A thesis submitted in partial fulfillment
of the requirements for the degree of
Master of Science in Cell and Molecular Biology

by

Meaad Alqahtany
King Abdul-Aziz University
Bachelor of Science in Biology (Microbiology), 2014

May 2019
University of Arkansas

This thesis is approved for recommendation to the Graduate Council

Yong Wang, Ph.D.
Thesis Director

Colin Heyes, Ph.D.
Committee Member

Mary Savin, Ph.D.
Committee Member

Abstract

Silver nanoparticles (AgNPs) and ions (Ag^+) can be the new generation of antibiotics due to their antimicrobial effects against bacteria and other microbes. Many studies have shown that AgNPs and Ag^+ suppress the growth of bacteria and damage the cell walls of the microbes; therefore, treating bacterial cells with AgNPs may be a promising method to terminate multi-resistant bacteria. In this work, the effect of AgNPs with two different surface coatings on the spatial reorganization of histone-like nucleoid structuring (H-NS) proteins in *Escherichia coli* bacteria was investigated using quantitative super-resolution fluorescence microscopy to understand the toxicity and antimicrobial mechanism of AgNPs. H-NS protein is one of the major DNA-associated proteins in bacteria, serving as a universal regulator. AgNPs inhibited the bacterial growth, changed the morphology of bacteria, and disturbed the membrane of bacteria. More importantly, treating bacteria with AgNPs led to spatial reorganization of H-NS proteins because of the released Ag^+ ions and changes in the clustering behavior of H-NS proteins. Spatial reorganization at the molecular level was quantified using algorithms based on Voronoi diagrams and tessellation. In addition, Ag^+ ions released from AgNPs led to the formation of larger and denser clusters of H-NS protein centered in the bacteria. As H-NS is a DNA binding protein, denser clustering of H-NS proteins is likely related to the DNA condensation, which was reported previously in the literature.

Acknowledgments

First and foremost, many thanks to Dr. Wang, my adviser for believing in me and giving me this excellent opportunity to work with him and conduct my research under his supervision with the rest of the lab members. I would like to thank him for mentoring me during these two years and supporting me since day one, on both levels, scientifically and academically. Also, many thanks to the lab team and to everyone who was involved in finishing this project. Thank you very much for making this journey enjoyable and advantageous.

Second, many thanks to my committee members: Dr. Mary Savin and Dr. Colin Heyes for their valued comments and suggestions on my research and thesis.

Furthermore, I would like to thank my family and my support system for the love and the great wishes that they kept sending to me overseas. Thank you for being by my side all the way even though we were on two different sides of the planet.

Special thanks to my aunt Misha who has been my number one role model in life and whom I kept growing up to be like. Thank you for the unconditional love, the unbelievable support and for the unforgettable memories that we had all over the years.

Last but not least, no matter what I say, I can’t thank enough King Abdullah bin Abdul-Aziz for making this possible and for initiating this excellent scholarship program. All appreciation and respect to his majesty for introducing a new era of education to the youth of the Kingdom of Saudi Arabia and for sending us to study all over the globe.

Dedication

To the bravest woman, I've ever known in my entire life. To the woman who I'm proud to be blood to her. This work is dedicated to you. May God rest your soul in peace.

Table of Contents

Chapter One

Chapter Two

Chapter One

1. Introduction

1.1 Antibiotics and Antibiotic Resistance

Since the discovery of penicillin by Alexander Fleming in 1928, antibiotics have been effective for killing microbes and treating infections (Tan & Tatsumura, 2015). Antibiotics such as streptomycin and penicillin are chemical substances produced by many microorganisms and fungi that can kill bacteria (Rayamajhi, Cha, & Yoo, 2010). Antibacterial treatment has revolutionized the medicine concept and saved the lives of patients. The importance of antibiotics is determined by the efficacy of targeting bacterial cells inside the human body without invading the human tissues (Gould & Bal, 2013). Antibiotics have several action mechanisms in terminating bacterial cells such as inhibiting DNA replication, blocking translation, inactivating 70s ribosomal complex formation, and inhibiting protein synthesis (Wang, Du, Zhao, Yan, & Gu, 2009). Many surgeries such as organ transplantation could not be conducted successfully without antibiotics (Bradford, 2001). Antibacterial activity can damage bacterial cell membranes causing leakages of vital cellular components, which will lead to cell death (Bradford, 2001). Antibiotics contributed significantly to controlling many diseases and to decreasing the morbidity level (Fair & Tor, 2014). Antibiotics have controlled infectious diseases caused by bacteria; however, bacteria have been gaining resistance against many antibiotics (Rayamajhi, Cha, & Yoo, 2010).

Antibiotics have served humanity well until bacteria started to develop resistance. Thus, despite the considerable advantages of using antibiotics, antibiotics resistance has become a global threat. For example, bacteria may produce enzymes to degrade antibiotics. Therefore, the future of using antibiotics to destroy bacterial cells is less optimistic (Aminov, 2010). Antibiotic-

resistant bacteria have become, over the past years, a serious health issue, and the number of the approved antibiotics for treating resistance bacteria by the US Food and Drug Administration has decreased significantly (Ventola, 2015). Eventually, it is likely that the decrease in the number of approved effective antibiotics will cause an increase in the mortality and morbidity rate in humans' lives. Therefore, the world is facing a serious health threat due to the ability of bacteria to overcome antimicrobial products. Bacterial resistance against antibiotics has been raising "red flags" indicating a crisis. The impacts of infection are harder to treat because of bacterial resistance, and it is worth finding new antibacterial alternatives. As a result, there is an urgent need to introduce new agents that can effectively kill bacteria and harmful microbes. One promising candidate is silver nanoparticles (AgNPs), which have been shown to suppress the growth of bacteria and kill bacteria, thus paving the way to new generation of antibiotics (Rai, Yadav, & Gade, 2009)

1.2 Silver and Silver Nanoparticles as Alternatives to Antibiotics

1.2.1 Background of Using Silver and Silver Nanoparticles

Silver has been used as an antimicrobial agent even before microbes were known as a cause of infection (Alexander, 2009). For many years, silver products were used as an antimicrobial agent in open wounds caused by burns and diabetic ulcers (Silver, Phung, & Silver, 2006). Over many decades, silver was used in water and food containers to retain freshness for an extended period (Alexander, 2009). A method used to prevent bacteria from contaminating water or milk during long distance travel involved throwing silver coins into the containers (Alexander, 2009). One important criterion for use of silver is the ability to release silver ions in aqueous solutions. Silver ion (Ag^{+}) is a bioactive ion that can interact directly with cell

membrane proteins and functional enzymes; thereby, the toxicity of metallic silver and silver nanoparticles is proportional to the concentration of silver ions (Hipler & Elsner, 2006).

Nanoparticles (NPs) are particles with size at the nm scale. They can be synthesized using multiple ways to form different shapes and sizes of nanoparticles; the typical diameter can range from 1 to 100 nm. One of the first use of nanoparticles as an antibiotic was developed by Professor Peter Paul Speiser and his graduate students in the late 1960s, who were among the first scientists using nanoparticles as a drug therapy against bacterial infections (Kreuter, 2007). Dr. Speiser used nanoparticles as a carrier for a drug to be released inside the body within the bloodstream (Kreuter, 2007). Prof. Speiser and his graduate student Jorg Kreuter enhanced nanoparticle proprieties to be used in vaccinations in the 70s and early 1980s (Kreuter, 2007).

Later, a fellow professor from Melbourne, Australia joined Prof. Speiser's group and worked with them before going back to Melbourne to initiate his team and also become one of the first founders nanoparticle use (Kreuter, 2007). Richard Oppenheim worked on developing nanoparticle methods of synthesis from 1977 through 1978 (Kreuter, 2007). Many other scientists, such as Patrick Courveur and Robert Gurny, continued developing nanoparticle formation and expanding the treatment applications of using nanoparticles for drug delivery (Kreuter, 2007).

Nanoparticles can be synthesized from different metals, including gold, silver, copper, zinc, magnesium, etc. Silver nanoparticles were used in the experiments conducted in this project, as described in details later in the thesis. The rationale for choosing silver nanoparticles is that silver nanoparticles have been the most effective against bacterial cells, viral cells, and some eukaryotic micro-organisms. The effectiveness of silver and its compounds have been seen on microbes including bacteria, viruses and eukaryotic microorganisms (Gong et al., 2007).

1.2.2 Silver Nanoparticles as an Antimicrobial Agent

Silver ions (Ag^+) have suppressed the growth of many bacteria including *Escherichia coli* cells. According to Jung (2008), silver ion at 0.2 to 0.05 ppm over 24 hours reduced the growth rate of *S. aureus* and *E. coli* by conventional plate counting. The total number of both bacterial strains were reduced by over 5 Log_{10}CFU/ml. Silver ions (Ag^+) affect cell morphology and change the external shape of treated cells (Jung et al., 2008). The presence of silver ions in the surrounding media can shrink and rupture bacterial cells (Jung et al., 2008). Binding of silver ions to chloride ions reduces the antibacterial efficacy of AgNPs indicating that AgNPs are responsible for the changes to *E. coli* cells. Another mechanism of antibacterial activity of AgNPs is the induction of reactive oxygen species (ROS), such as hydrogen peroxide, hydroxyl radical and superoxide anion, which cause major disruption of the cellular respiratory processes and eventually lead to cell burst (Dakal, Kumar, Majumdar, & Yadav, 2016). Once AgNPs move inside the cells via endocytosis, they cause major damage and dysfunction for nucleic acids and proteins in the cells, which lead to production of more ROS (McShan, Ray, & Yu, 2014).

Some studies show that silver nanoparticles can be a promising alternative for treating infections caused by multi-drug resistant bacteria (Rai, Deshmukh, Ingle, & Gade, 2012). In addition, studies report that silver nanoparticles could be useful for treating biofilms. The formation of bacterial biofilms helps the bacteria to survive in harsh environments and resist antibiotic treatments. However, upon exposure to silver nanoparticles, the structure of the biofilm and the extracellular polymeric substances within the biofilm display a reduction in attachment strength (Schmidt, 2017). Thus, AgNPs may be an effective disinfection method for medical equipment in hospitals such as for catheters. Silver nanoparticles are chosen over the silver ions because of the development of nanotechnology provided different methods for the

modification of the chemical and physical structure of silver, which may increase its antibacterial potential (Kędziora et al., 2018). As the use of silver ions is limited as an antimicrobial agent due to it is solubility in biological and environmental media that contains Cl^-, silver nanoparticles serve as good candidate. Silver nanoparticles dispersed in polymers are much more stable than silver ions in polymer and often show greater antimicrobial properties due to their extremely large surface area-to-volume ratios. Most importantly, silver nanoparticles and polymer form nanocomposites that largely decrease the cytotoxicity of nanoparticles, but still release ions exhibiting excellent antibacterial activity. In addition, silver nanoparticle can be modified to manipulate the chemical and physical properties; however, it is hard to control silver ions in the solutions.

1.2.3 Antimicrobial Action Mechanisms of Nanoparticles and Silver Nanoparticles

Several antimicrobial mechanisms of AgNPs have been proposed. However, the exact mechanism is still under debate and not fully understood. Several potential fundamental mechanisms exist depending on the nanoparticles' characteristics and engineering. One possible mechanism requires the direct attachment between nanoparticle and cell membrane for cell inactivation. In terms of cell's membrane and NP interaction, there are two proposed pathways for the cell membrane damage or deconstruction. First, the adhesion of nanoparticles to the membrane of the bacteria allows local interactions of the nanoparticles with the cell membrane components such as lipids and amino acids, which can cause a local deconstruction in the cell membrane and lead to lipid deformation. This process may create pores in the membrane and cause a massive leakage of intracellular components. The second pathway is the passive adhesive membrane translocation. Once the nanoparticles bind to the cell membrane, the cell envelopes

the foreign particles by forming a lipid extraction vesicle, which is either transported outside the cell or inside the cell (Chen & Bothun, 2014).

Another key potential mechanism is that nanoparticles penetrate through the cell membrane and lead to more damage. Once the nanoparticles are inside the cell, relatively small size NPs (1 – 10 nm) can interact with sulfur and phosphorus materials, such as DNA and some of the structural proteins (Morones et al., 2005). Furthermore, metallic nanoparticles can release ions that may interact with thiol groups, resulting in inactivation of proteins. The thiol groups may be responsible for attachment of nanoparticles to the cell membrane. Silver ions released from silver nanoparticles can interact with DNA, inhibiting replication, causing DNA condensation, and inactivating other cellular proteins (Tenaillon, Skurnik, Picard, & Denamur, 2010). In addition, nanoparticles may disturb, denature and destabilize the biological activity of proteins in bacterial cytoplasm (Escherich, 1988).

A third antibacterial mechanism of AgNPs is that the nanoparticles can interact with bacterial cells by changing biochemical pathways. As an example, AgNPs can modify tyrosine phosphorylation, preventing cellular signaling in gram-negative bacteria and affecting cell growth (Shrivastava et al., 2007). It has shown that AgNPs can disrupt biofilms, one of the most important characteristics of bacterial virulence.

The toxicity of silver nanoparticles depends on many factors, including the polymer coating, surface charge, size, and shape. A study using silver nanoparticles of different shapes, including triangular and circular shapes, reported that bactericidal activity varied for different shapes. Greater suppression of bacterial growth occurred with triangular nanoparticles compared to spherical AgNPs at the same concentration and the toxicity of AgNPs increased as the size of NPs decreased (Pal, Tak, & Song, 2007). Smaller NPs (1 to 10 nm) may be able to pass through

the cell membrane more easily and thus affect the cells more effectively. The surface charge of the nanoparticles can also play an important role in the toxicity of the nanoparticles. For example, Schiavo et al. (2017) synthesized nanoparticles with coating agents to increase the surface charges, measured the toxicity of the nanoparticles on microalgae, and observed that coated nanoparticles are more toxic than uncoated ones.

1.2.4 Applications of Using Silver Nanoparticles

In general, the biological effect of silver is believed to be due to the free silver ion, which smaller silver particles release silver ions faster, leading to a higher toxicity due to higher effective silver ion concentration. Therefore, silver nanoparticles have been utilized in many applications. For example, AgNPs have been used in the health care industry, food storage, water filtration, and many biological and biomedical applications (Zhang, Liu, Shen, & Gurunathan, 2016). AgNPs can prevent algal growth in swimming pools, intervene in cosmetics products, and, most recently, have been used as the new generation of antibiotics (Gehrke, Geiser, & Somborn-Schulz, 2015; Rai et al., 2009) to treat many infectious diseases caused by bacteria, fungi, and viruses (Zhang et al., 2016). AgNPs were also used as an alternative treatment for cancer instead of chemotherapy to avoid side effects (Thorley & Tetley, 2013). Furthermore, AgNPs have been developed into biosensors (Loo, Lowery, Halas, West, & Drezek, 2005).

1.3 Motivation of the Study

As mentioned, the antimicrobial mechanisms of AgNPs at the cellular and molecular levels are not completely understood. This is the case partly due to the small size of bacteria, multiple copies of proteins, and the lack of right tools. A typical *E. coli* bacterium has a diameter

of 500 nm, while conventional optical microscopy has a spatial resolution of 250 nm due to the diffraction limit. If there are multiple copies of the same molecule inside a single bacterium, these molecules cannot be resolved. Therefore, an emerging tool, termed super-resolution fluorescence microscopy, was used in this study.

1.3.1 The Diffraction Limit Challenge

According to Ernst Abbe (1873) and Lord Rayleigh (1896), the resolution of an optical microscope is roughly half the wavelength of the light used for the microscope. As light is a wave, it diffracts; therefore, no matter how small an object is, it would appear as a spot with a size of $d = \frac{\lambda}{2}$. In other words, it is difficult for conventional optical microscopes to distinguish two molecules separated by a distance (d) that is less than half the wavelength (λ) (Huang, Babcock, & Zhuang, 2010). Typically, because optical microscopy uses visible light, with a wavelength ranging from 400 nm to 700 nm, the spatial resolution is between 200 to 350 nm. Therefore, conventional optical microscopes cannot resolve two biological molecules separated at less than 200 nm.

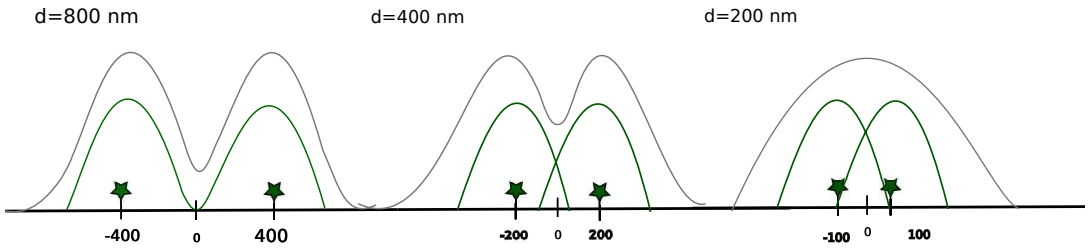

Figure 1. Schematic illustration of the difference between resolved molecules and unresolved molecules due to the limit of the diffraction: on the left are two spots widely separated from each other ($d = 800\ nm$), in the middle are two spots showing the overlap between the two focal spots once the distance decreased, and on the right is the formation of one focal spot once the distance between the two molecules is 200 nm or less.

Figure 1. illustrates this concept in details. If two molecules are separated by $d = 800$ nm, the two spots can be easily resolved. However, once the distance between the two molecules started to decrease ($d = 200$ nm), the two spots will become one spot, and the two spots cannot be resolved.

1.3.2 The Solution: Super-Resolved Fluorescence Microscopy

The main approach used in this study is a powerful technique called super-resolved fluorescence microscopy. There are different types of super-resolution fluorescence microscopy, and the one used in this study is based on single-molecule localization. The photons emitted from a single molecule (i.e., a point source) form a near-Gaussian function in the image plane of the microscope, which is known as the point-spread function (PSF). By fitting the PSF with a 2D Gaussian function, the center of the PSF (i.e., the position of the molecule) can be obtained. The precision for the localization is roughly.

$$\Delta_{loc} = \frac{\Delta}{\sqrt{N}}$$

where Δ is the size of the PSF ($\sim\lambda/2$) and N is the number of photons (Huang, Bates, & Zhuang, 2009). With sufficiently high number of photons, the localization precision can reach 1-10 nm (Balzarotti et al., 2017)

Super-resolution fluorescence microscopy based on single-molecule localization have different sub-types, including stochastic optical reconstruction microscopy (STORM), photo-activated localization microscopy (PALM) and fluorescence photoactivation localization microscopy (FPALM) (Betzig et al., 2006; Rust, Bates, & Zhuang, 2006). In this study, FPALM was used (Hess, Girirajan, & Mason, 2006), which can resolve molecules with separations of a few nanometers by using genetically expressed photoactivatable fluorescent probes (Betzig et al.,

2006; Thorley, Pike, & Rappoport, 2014). The photoswitchable fluorescent probes are the key to single-molecule localization imaging and can be manipulated and activated by light (Fürstenberg & Heilemann, 2013). In each frame during the imaging, only a few fluorophores are photoactivated, allowing localization of those molecules with great precision. One can record a movie in which different molecules are photoactivated and localized in different frames. This process will eventually allow localizations of most molecules of interest, and construction of super-resolved images based on the localizations of these molecules (Figure 2).

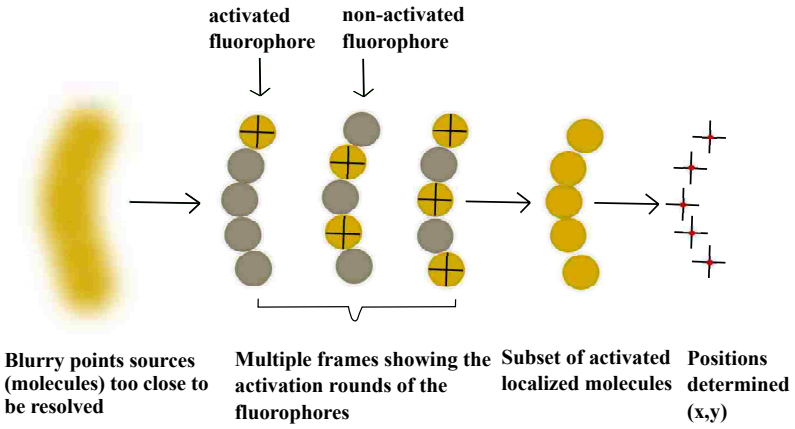

Figure 2. The sequence of the process of determining the single molecules coordinates

Our super-resolution fluorescence microscope (Figure 3) allowed investigation of the positions of the targeted proteins and how those proteins were affected by the AgNP treatment based on the single-molecules' coordinates. A typical achievable spatial resolution with super-resolution fluorescence microscope is ~20 nm, more than 10 times better than conventional microscopy.

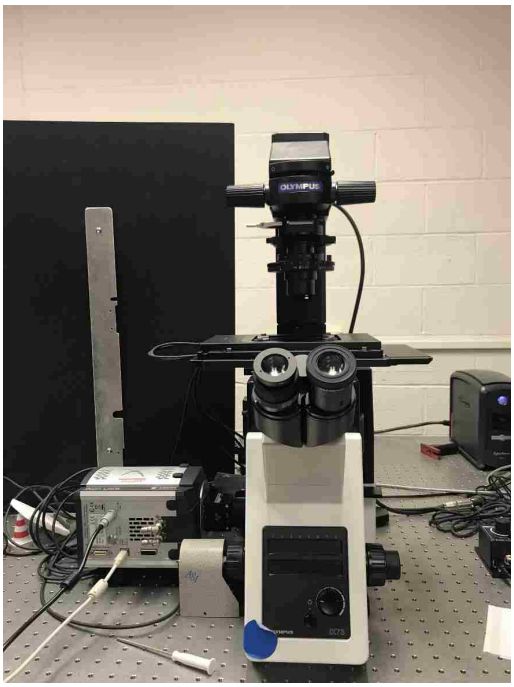

Figure 3. Super-resolution fluorescence microscope used in Dr. Wang's Lab.

1.4 Model System of the Study

1.4.1 *Escherichia Coli*

The model system used in this study is *E. coli* bacteria, which was discovered in 1885 by Theodor Escherich, a microbiologist from Germany (Tenaillon et al., 2010). *E. coli* is a gram-negative rod-shaped bacterium. It is the most studied and well-known bacteria. *E. coli* is a part of the normal microflora of the gastrointestinal tract in humans and animals, and it can be found in water, soil and food (Figure 4). The presence of *E. coli* in water is an indicator of water contamination with feces. *E. coli* is a facultative anaerobic bacteria, meaning the bacterium respires in the presence or the absence of oxygen (Tenaillon et al., 2010)

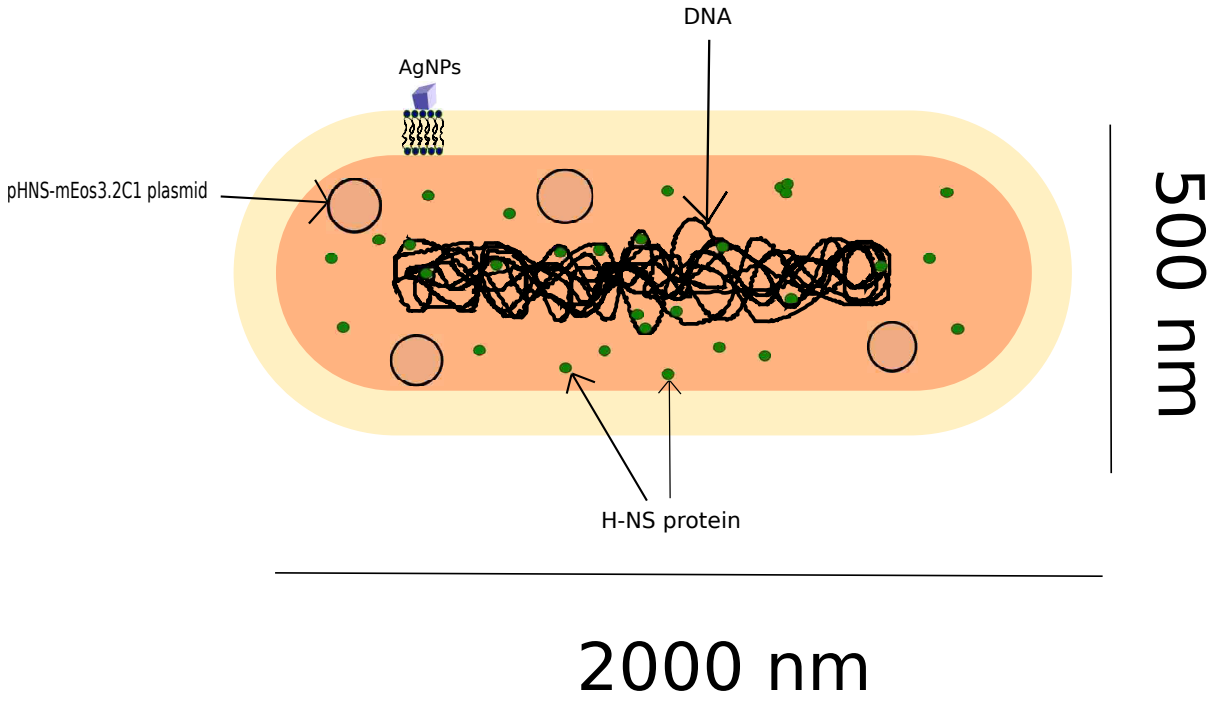

Figure 4. *E. coli* cell illustration showing the main components of the cell

E. coli is an opportunistic pathogen and it grows easily on many different culture media (Escherich, 1988). The size of an *E. coli* is about 2 µm in length and 0.5 µm in diameter; however, these measurements can vary based on the conditions of the strain (Tenaillon et al., 2010). *E. coli* is a motile bacterium that has flagella to facilitate movement in viscous liquid environments. Being a commensal bacterium in the gut of warm-blooded animals, *E. coli* can be an opportunistic pathogen, invade the human body, and be the cause of many diseases including diarrhea, death of infants, urinary tract infections and colitis.

The *E. coli* strain used in this study is derived from *E. coli* K-12 strain, which is considered as the most-used bacterial strains in the experimental field because of many advantages. One of the advantages is that scientists have understood *E. coli* K-12 genetics. A reason for preferential use of *E. coli* K-12 strain is the genetic modification method is easier than

for other strains. Also, *E. coli* K-12 is a safe host cell for a successful gene cloning and expression experiments (Kuhnert, Nicolet, & Frey, 1995).

To allow super-resolution fluorescence imaging, photoactivatable fluorescent proteins needed to be fused with the protein of interest. This introduction was done by supplementing the bacterial strain with a plasmid encoding the fusion protein (described below) and knocking out the gene of the protein of interest from the bacterial genome. The knock-out strain is from the Keio collection, which is a set of single-gene knockout of all the unnecessary genes in *E. coli* K-12 (Baba et al., 2006). Out of the 4288 targeted genes, 3985 genes were mutated and the result was two independent mutants for every deleted gene. The total number of the Keio collection knockout strains is 7970 (Baba et al., 2006).

1.4.2 Histone-like Nucleoid Protein (H-NS)

The H-NS protein is a histone-like nucleoid structuring protein (H-NS) and is one of the bacterial proteins associated with DNA. Due to the major role that H-NS proteins play in the regulation of gene expression in bacteria, it was chosen as the focus of this study (Dorman, 2004). Investigating the changes caused by AgNPs to H-NS proteins will lead to a bettering understanding about the DNA, which is the platform of proteins' activity. In addition, studying H-NS proteins' reorganization will help us understand bacterial resistance and how bacteria survive harsh environments because H-NS protein functions in gene silencing (Dorman, 2004). H-NS protein is a widely distributed within gram-negative bacteria and is one of the most abundant proteins in *E. coli* (Bloch et al., 2003).

The molecular weight of histone-like nucleoid structuring protein (H-NS) is 15.5 kDa, with 137 amino acids in length (Dorman, 2004). The H-NS protein forms a dimer, each

monomer consists of two domains, the oligomerization domain and the DNA-binding domain (Dorman, 2004). The oligomerization domain includes 83 amino acids, which are located in the N-terminal. It is important for oligomerization and the interaction among proteins. The DNA-binding domain contains 54 amino acids in the C-terminal and it allows the protein to bind to DNA. (Singh, Milstein, & Navarre, 2016). The two domains are connected by a linker (Chen, Zaro, & Shen, 2013). The H-NS proteins preferably bind to A-T rich regions on DNA and the bacterial genome (Navarre et al., 2006).

The DNA compaction and condensation are mainly regulated by H-NS, as much as its responsible for the DNA unfolding. Over-expression of H-NS results in DNA condensation, which will lead to the cell death eventually. On the other hand, the DNA is widespread and uncondensed in the absence of H-NS (Dame, 2000). Thus, H-NS can compact and uncompact DNA, so it is a gene silencer which is responsible for 5% of the open reading frames of the whole genome of *E. coli* (Hommais et al., 2001). Most of the genes that are regulated by H-NS proteins are responsible for cell virulence and adaptation toward environmental conditions (Hommais et al., 2001). The H-NS protein is responsible for juxtapositions of the bacterial genome and the notable condensation (Wang, Li, Chen, Xie, & Zhuang, 2011). The H-NS proteins can modulate transcription processes by forming large structures of nucleoprotein (Tupper et al., 1994).

1.4.3 Plasmid and Photoactivatable Fluorescent Protein

The main strain that was used for this work was K-12ΔH-NS supplemented with the pHNS-mEos3.2C1 plasmid. The pHNS-mEos3.2C1 plasmid encodes the genes producing H-NS

protein and making it fluorescent. The mEos3.2 is a protein that can be activated by a 405 nm laser to be fluorescent, which facilitates detection of the H-NS protein (McKinney, Murphy, Hazelwood, & Looger, 2009). Fluorescent protein fusion (mEos3.2) is the tool for investigating the H-NS protein clustering and reorganization.

The monomeric mEos3.2 is an engineered photoactivatable fluorescent protein used for super-resolution microscopy. It is widely used because it provides the highest photon output among the photoactivatable fluorescent proteins (Zhang et al., 2012). The fluorescent protein mEos3.2 has been shown as an excellent applicant for high-resolution imaging for the H-NS protein (McKinney et al., 2009). Having mEos3.2 genetically encoded means that the labeling efficiency is highly effective, which is important because the photo-activation efficiency is a critical factor for the data interpretation (Durisic et al., 2014). Among the two typical types of probes that are used for the localization based super-resolution imaging, mEos3.2 is considered an irreversible probe. The irreversible photo-activation means that each molecule will be detected and counted once, even though, the probe is activated many times (Durisic et al., 2014).The protein mEos3.2 can be irreversibly photoactivated from a dark state to a bright state (Fürstenberg & Heilemann, 2013).

1.5 Hypothesis and Aim of the Research Study

Multi-drug resistant bacteria have become a serious health problem and H-NS proteins paly major role in regulating bacterial genes expression including some of the multi-drug exporter genes. Therefore, the focus of this research is the study of the behavior of the H-NS proteins and how AgNPs affect the spatial organization of H-NS proteins. I hypothesize that subjecting bacteria to AgNPs will result in changes in the spatial organization of H-NS proteins,

which will in turn affect gene regulation and various cellular processes. Another hypothesis is that the spatial reorganization caused by AgNPs depends on the surface coatings.

The goal of this study is to investigate and quantify the spatial reorganization of H-NS proteins in bacteria when subjecting the bacteria to AgNPs with two different surface coatings. I aim to determine the extent to which the spatial organization of H-NS proteins depends on the exposure of silver nanoparticles. In addition, I aim to measure the dependence of the spatial reorganization of H-NS proteins on the treatment time.

Chapter Two

2. Experiments and Methods

2.1 Synthesis and Characterization of Silver Nanoparticles

2.1.1 Synthesis of Silver Nanoparticles

Silver nanoparticles were synthesized by the following polyol method: 50 mL of ethylene glycol (EG) was added to a 250-mL round-bottom flask equipped with a stir bar and placed in an oil bath at 150°C (Wang et al., 2013). After the temperature equilibrated (30~45 min), EG solutions of 0.6 mL of 3 mM NaHS, 5 mL of 3 mM HCl, 12.5 mL of polyvinylpyrrolidone (PVP), and 4 mL of 282 mM AgTFA (silver trifluoroacetate) were sequentially added to the reaction flask. Once the localized surface plasmon resonance (LSPR) peak reached ~440 nm (~35 min after addition of AgTFA), the reaction was quenched in an ice bath. Upon cooling, the product was collected by adding acetone to the reaction solution at a ratio of 5:1 and centrifuging at 6,000 rcf for 10 min. The resulting pellet was purified twice with distilled water and collected by centrifugation at 20,000 rcf for 10 min, and re-suspended in 10 mL of distilled water for future use. The other type of silver nanoparticles was synthesized based on the PVP-AgNPs patch by applying a ligand-exchange reaction. Branched PEI was mixed with pre-made PVP-capped AgNPs (Figure 5).

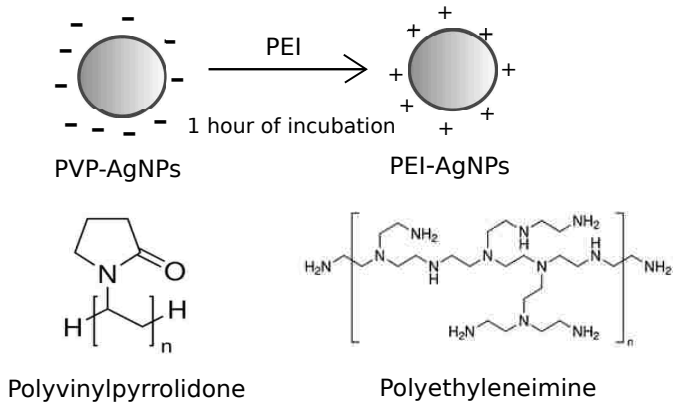

Figure 5. A general scheme of the ligand-exchange process of PVP-AgNPs into PEI-AgNPs.

The molar ratio of PEI was 1:1,000,000 to the molar ratio of the PVP in 15 ml as the final volume. The reaction mixture was incubated for 1h at room temperature under magnetic stirring. The color of the AgNPs started to change after 1 hour from dark yellow to reddish, which was an indicator for the reaction of the ligand-exchange. The mixture was centrifuged at a high speed around 14,000 rpm for half an hour. Two steps of washing were performed on the precipitations and the final product was mixed in 5 ml of distilled water and stored at room temperature in the dark.

2.1.2 Characterization of Silver Nanoparticles

Because the properties of silver nanoparticles significantly impact the biological properties of bacterial cells, many physicochemical characteristics have to be measured before utilizing AgNPs in experiments (Zhang et al., 2016). The AgNPs' size in aqueous solutions and dried particles, average shape, surface charge, accumulation and dispersity are the main characteristics that were determined for the silver nanoparticles synthesis and characterization. The AgNPs characterization process included multiple techniques to ensure the functionality of the synthesis nanoparticles such as UV-vis spectroscopy, transmission electron microscopy (TEM), dynamic scattering light (DSL), and flame atomic absorption spectroscopy (AAS).

2.1.2.1 UV-vis Spectroscopy

UV-vis spectroscopy provides the first characterization of AgNPs to ensure the quality of the synthesis and stability of the synthesized nanoparticles (Sastry, Patil, & Sainkar, 1998). The AgNPs interact strongly with a specific wavelength, which gives them a unique optical property (nanoComposix, 2012) The observational peak of AgNPs have been well documented

previously for many metal nanoparticles of different size (Sastry et al., 1998). The AgNP samples were diluted 1:1000 in a 3-ml tube; then 2 ml were transferred to a cuvette. The cuvette was placed in the UV-vis spectrometer after applying a distilled water blank.

2.1.2.2 Transmission Electron Microscopy (TEM):

The size and morphology of the synthesized AgNPs are characterized by TEM (Lin, Wang, & Sridhar, 2014), which provides fine spatial resolution for quantifying the grain size of nanoparticles (Lin et al., 2014). Generally, in the particle technology, a non-spherical nanoparticle size is defined as an equivalent diameter (nm) of spherical particle that shares the same physical properties in the same environment such as diffusivity (Powers et al., 2006). The samples were prepared by drop-casting 3 μL of the aqueous AgNP suspension onto a carbon-coated copper grid and left to dry overnight at room temperature. The images were captured on a transmission electron microscope (JEOL JEM-1011) with an accelerating voltage of 100 kV. The NIH ImageJ software was used to measure the sizes of the nanoparticles.

2.1.2.3 Dynamic Light Scattering (DLS):

Dynamic light scattering is DLS is a common, light and particle interaction technique used to determine the distribution of hydrodynamic size of the AgNPs in solution. Dynamic light scattering can probe to one nanometer (Lin et al., 2014). All samples were filtered through a 0.22-μm nylon syringe filter prior to DLS. The correlation in the intensity of the scattered light by the nanoparticles is a function of the hydrodynamic size and polydispersity index (PDI) of the nanoparticles (Figure 6) (Fissan, Ristig, Kaminski, Asbach, & Epple, 2014). Therefore, both the hydrodynamic size and PDI of the nanoparticles can be measured by DLS. Note that the size of

nanoparticles measured by DLS is expected to be larger than the size measured using TEM because the surface coating was taken into account in the DLS measurements. The same equipment can also be used to measure the zeta potential of the nanoparticles. Zeta potential is an indication of the surface charges of AgNPs. The typical range of the stability of nanoparticles' zeta potential is usually greater than +30mV if it is positively coated and less than -30mV of it is negatively charged (Zhang et al., 2008).

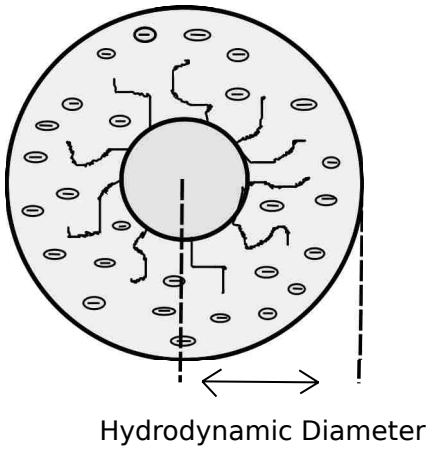

Figure 6. Demonstration of the Hydrodynamic diameter of AgNPs measured by DLS

2.1.2.4 Flame Atomic Absorption Spectroscopy (AAS):

Generally, AAS was used to measure the concentration of silver ions (Sharma et al. 2014). The AgNPs samples were dissolved in 2% of HNO3 to make ions. The final volume of the solution was 10 ml. AgNPs samples were placed in the shaker for 30 minutes, then measured (Haider & Mehdi, 2014).

2.1.3 Stability Measurements

The stability of AgNPs in bacterial growth medium was examined by measuring the changes in size and charge after incubating the nanoparticles in the medium for 24 hours.

Briefly, silver nanoparticles were diluted into distilled water and growth medium (M9GTC medium) to a final concentration of 40 μg/ml. The AgNPs were incubated in the medium (or water) for 24 hours at 37 ºC at 250 rpm in the shaking incubator. Positive control and negative control were applied simultaneously. The positive control was silver nanoparticle added to the solution and immediately measured, and the negative was solution only without any addition of the AgNPs. The zeta potential of AgNPs was measured using DLS, as described above, to determine the change in the surface charge and hydrodynamic size of the AgNPs.

2.1.4 Determination of Ion Release from AgNPs

The release of silver ions from AgNPs was determined by measuring the concentration of silver ions in the supernatant using the flame atomic absorption spectrometry (AAS) (Welz, 1999). Silver nanoparticles were diluted in distilled water or bacterial growth medium at a final concentration of 40 μg/ml. The samples were incubated at 37°C in a shaking incubator (250 rpm) for 24 hour, followed by centrifugation at 15000g for 15 minutes to collect supernatant. This process was repeated three times and the concentration of silver ions in the final supernatant was measured. Negative controls were measured by using distilled water or growth medium.

2.2 Growth and Cultivation of *E. coli*

2.2.1 Strain and Plasmid

A K12-derived *E. coli* strain was used in this study. This strain has the *hns* genes knocked out (K12ΔHNS) and is supplemented with the plasmid (pHNS- mEos3.2C1). This plasmid provides the *hns* genes fused to mEos3.2 fluorescent protein (Figure 7). In addition, it is photo-switchable, facilitating super-resolution fluorescence microscopy.

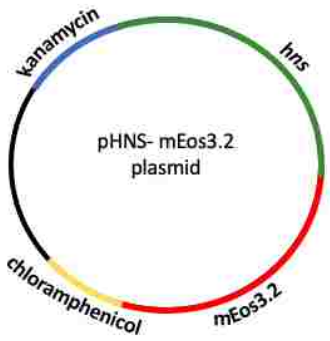

Figure 7. General scheme of the main components of the plasmid (pHNS-mEos3.2)

2.2.2 Growth Conditions

Bacterial cells K12ΔHNS/pHNS- mEos3.2 were obtained from the lab stock stain collection and grown on agar and Luria-Bertani (LB) plates supplemented with 50 μg/ml of kanamycin and 34 μg/ml of chloramphenicol. From the agar plates, one colony was inoculated into 5 ml of defined M9GTC medium, which contains 1% glucose, 0.1% casamino acid, 0.01% thiamine, and M9 salts supplemented with appropriate antibiotics. The M9 minimal salts is a highly-referenced microbial growth medium used for the cultivation of *E. coli* usually supplemented with amino acids and vitamins as needed (Sigma-Aldrich). The liquid culture was grown overnight at 37°C in a shaking incubator (250 rpm). On the second day, the overnight culture was diluted in fresh medium to reach optical density (OD600) ~ 0.05. The fresh culture was grown again at 37°C until OD600 reached ~0.3, followed by adding AgNPs to the culture at a final concentration of 40 μg/ml (Figure 8). This concentration of AgNPs was chosen based on a previous research, where it was observed that 40 μg/ml of AgNPs can suppress the growth of bacteria for 12 hours (Haque et al., 2017a).

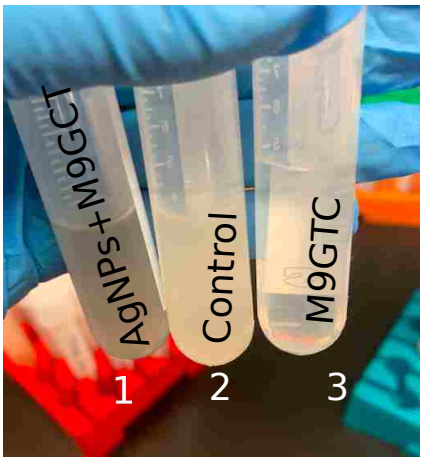

Figure 8. Three tubes showing the following, tube 1 is M9GTC media inoculated with *E. coli* cells and 40µg/ml of AgNPs added to it. Tube 2 is a control which has M9GTC with bacterial growth, and tube 3 only M9GTC media.

2.2.3 Determination of Antibacterial Activity

The experiments were reproduced twice and for each sample, multiple images (4-6) include bright field, and super-resolved imaging were imaged for each treatment time including untreated, 0 hours, 1 hour, 4 hours, 8 hours and 12 hours. The cells number per each sample ranged from 100 to 300 cells.

2.3.1 Bright Field Imaging

2.3.1.1 Measurement of Cell Length

Bright-field light microscopy was used to image the bacteria and determine cell lengths. The length of a bacterium was measured manually using ImageJ (NHI, USA) (Schindelin et al., 2012). Take a sample shown in Figure 9 as an example: a line from one pole to the opposite pole was drawn for each and every bacterium in the bright-field images. The length of line, measured by ImageJ in pixels, reports the length of the bacterium. In addition, a feature in ImageJ allows numbering of the cells to avoid possible duplication (Figure 10). One pixel equated to 0.160 µm

as shown in Figure 11.

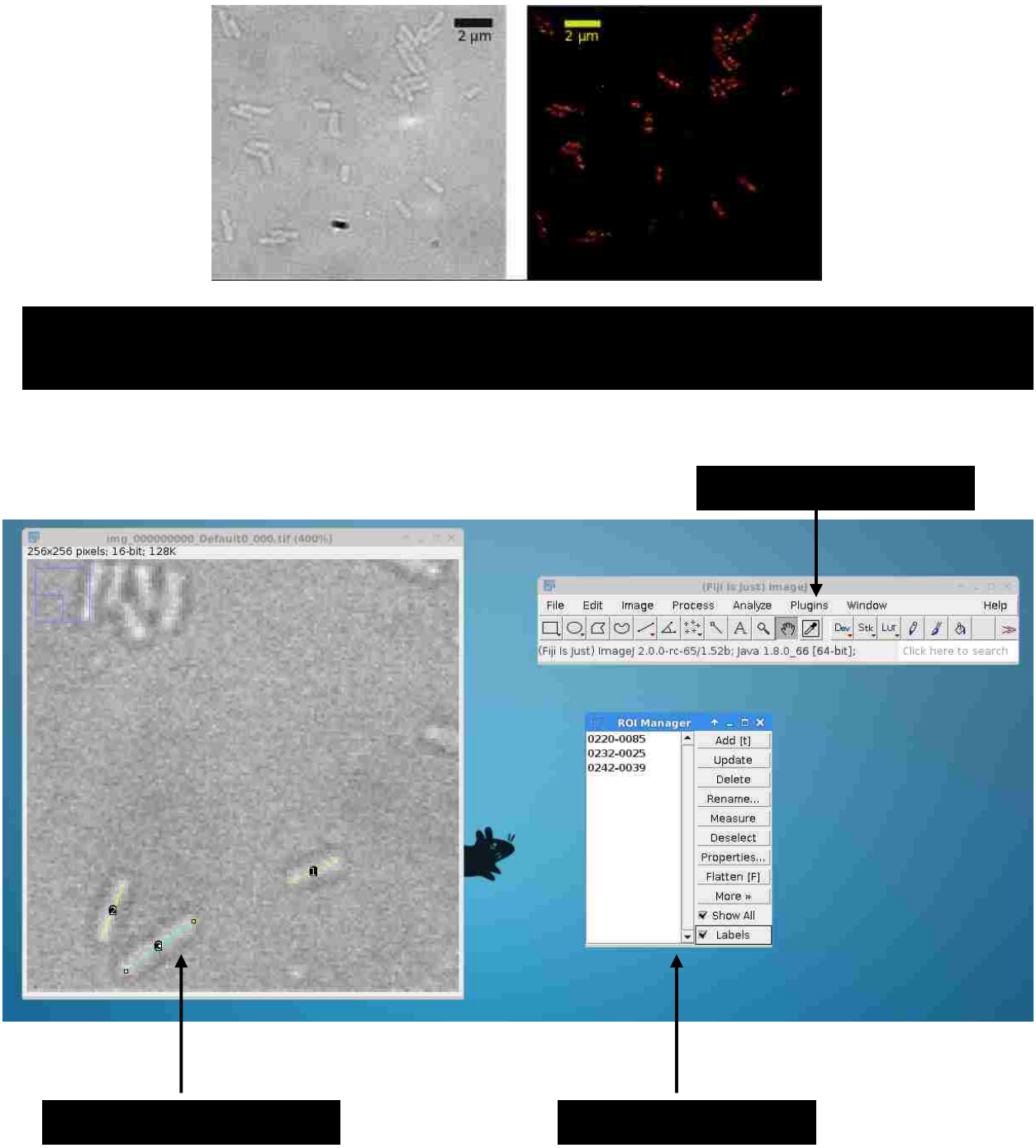

Figure 10. General scheme using ImageJ to measure cell length.

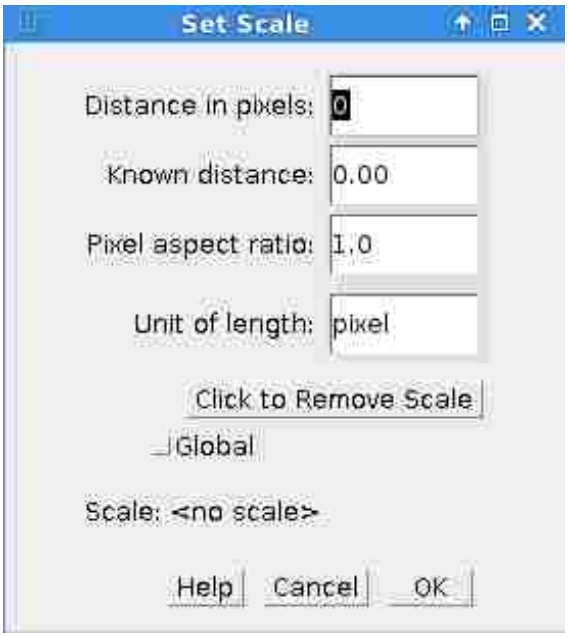

Figure 11. The measured unit of length was pixel

2.3.1.2 Statistics of cell lengths

The cell length distribution was displayed using one of the most common methods for summarizing data, the box plot (In & Lee, 2017), which visually presents the maximum and minimum values, upper and lower quartiles, and median. This 5-number summary is considered a quick and straightforward way to compare different distribution among datasets (Liu, 2008) The box is an indication for the upper and lower quartiles positions, and the area between them includes 50% of the data distribution. The lines, also known as the whiskers, present the extreme values of the distribution, maximum and minimum values. Finally, the crossbar intersecting the box is the median of the dataset. Microsoft Excel was used for the calculation and the data presentation. The differences among samples means were statistically calculated using ANOVA which was done for one data of one experiment result. One hundred randomly chosen cells were used to estimate the statistics.

2.3.2 Super-Resolved Microscopy Imaging

2.3.2.1 Preparation of H-NS Protein Samples

E. coli bacteria at OD600 ~0.3 were treated with AgNPs at 40 µg/ml for 0 hour, 1 hour, 4 hours, 8 hours, and 12 hours. The negative control did not contain the AgNPs treatment. At the end of the treatment, the cells were fixed by adding 37% formaldehyde to achieve a final concentration of 3.7% formaldehyde. The cells were placed in the shaking incubator at room temperature (23-25ºC) for 30 minutes followed by harvesting cells by centrifugation (1000g, 15 min). The supernatant was discarded and the cells pellets were re-suspended in 1 ml of 1X of phosphate-buffered saline (PBS) solution. Silver nanoparticles tended to precipitate at the bottom area of the micro-centrifuge tube forming a gray layer and the cells pellets were precipitated on top of the gray layer forming a white layer, which allowed re-suspension of the cells pellets without resuspending a large amount of the NPs (Figure 12). The washing step with 1X of PBS was repeated three times. The prepared samples were covered with aluminum foil, stored at room temperature, and imaged within 4 days.

Figure 12. Micro-centrifuge tubes showing the two layers formed upon settling of bacterial cells on top of AgNPs (left), and (right) the isolation of cell precipitate separately from AgNPs.

2.3.2.2 Preparation of Microscopic Slides Samples for Imaging

Cells were immobilized on a 3% agarose gel pad and placed facing a cleaned coverslip, surrounding the agarose pad was a rubber ring and covered with a cleaned glass slide. Coverslips and slides were soaked in deionized water and soap for 30 minutes while sonicated. Coverslips and slides were washed five times with deionized water and sonicated for another 30 minutes with sodium hydroxide (NaOH) to clean any residues off the surfaces. Finally, coverslips and slides were sonicated in 95% ethanol, washed a final time, and air-dried before use. The small 3% agarose pad was made on a clean coverslip, and was cut into a 3 mm x 3 mm square. Approximately 7-8 µl of each sample was added to the agarose pad surface and absorbed into the pad for 30 minutes before flipping gently onto a cleaned coverslip. The circular rubber ring was held onto the pad by gluing both faces of the ring and placing the glass slide on the other side of the ring (Figure 13). The sample was incubated for another 10 minutes in the dark to ensure cells were immobilized on the coverslip surface, which will face the microscope objective (Figure 14).

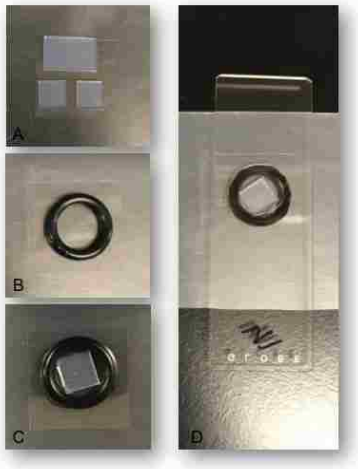

Figure 13. Sample (*E. coli* cells) preparation for imaging. A. 3% agarose pad sliced into squares on a clean coverslip and the cells were added on the top surface of the agarose. B. rubber ring placed on clean coverslip using stick glue. C. the agarose pad was flipped on the clean coverslip where the cells were facing the coverslip. D. clean slide placed and glued onto the rubber ring.

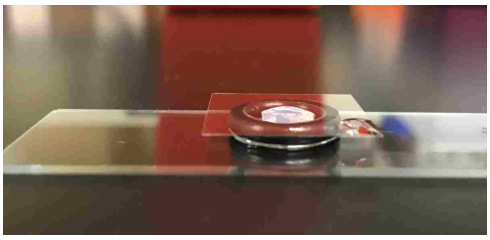

Figure 14. For the final setup of the microscopic slide, the slide will be inverted on the microscope oil immersion objective.

2.3.3 Super-Resolved Microscopy Processing

2.3.3.1 Imaging and Generating Data

The super-resolution fluorescence microscopy was constructed on an Olympus IX-8 inverted microscope supplied with an Olympus TIRF 100X N.A.= 1.49 oil immersion objective (Wang et al., 2016). Two imaging pathways were applied, bright field imaging and super-resolved imaging. For the super-resolved imaging, 20,000 frames were acquired for each field of view of the samples and the laser at 532 nm was at the greatest intensity (100%) for excitation, while the purple laser 405 nm was turned on for one frame for every 10 frames at a very low intensity (0.7%) (Betzig et al., 2006). The exposure time was 30 milliseconds (ms) and the pixel size for the acquired images was 160 nm. The acquisition for the sample imaging was performed using Micro-Manager (Hoboken, NJ) software. Each acquisition took about 15 min until most of the fluorescent proteins photo-bleached (Stuurman, Edelstein, Amodaj, Hoover, & Vale, 2010; Wolter et al., 2012a). The camera EMCCD (Andor, MA) objective was used to collect the emissions from the fluorescent proteins (Betzig et al., 2006).

2.3.3.2 Rapi*d*STORM

The collected movies were analyzed by a python script named rapi*d*STORM.

Rapi*d*STORM is a fast, open-source software for localization microscopy (Wolter et al., 2012). The variants from the acquired data are united in a single fitting routine by combining appropriate factors into the Gaussian point spread function (PSF) model to avoid any dim, blurry or broad unfitted emitted positions in all planes (Wolter et al., 2012). The threshold was set between 2000 to 10,000, and the pixel size was 160 nm. The localized spots which appeared to be distanced from each other with 10 nm in adjacent frames were considered a single molecule (Coltharp, Kessler, & Xiao, 2012). The remaining spots were further analyzed using another technique.

Rapi*d*STORM requires an input of a threshold for detecting spots. Experimentation and experience are typically needed to decide an appropriate value for the threshold. A threshold set too low will result in more false-positive spots (i.e., generating "junk" data), while a threshold set too high will lead to missing true-negative spots (i.e., throwing away wanted data). To address this problem, the Rapi*d*STORM analysis was done using a wide range of thresholds between 2000 and 10,000, and plotted the number of localizations vs threshold (Figure 15). A twist in the curve was observed in this plot. This twist indicates that less "junk" data were produced from this point. Therefore, the threshold slightly above the kink was selected. More specifically, 5000 was chosen for the threshold in this study.

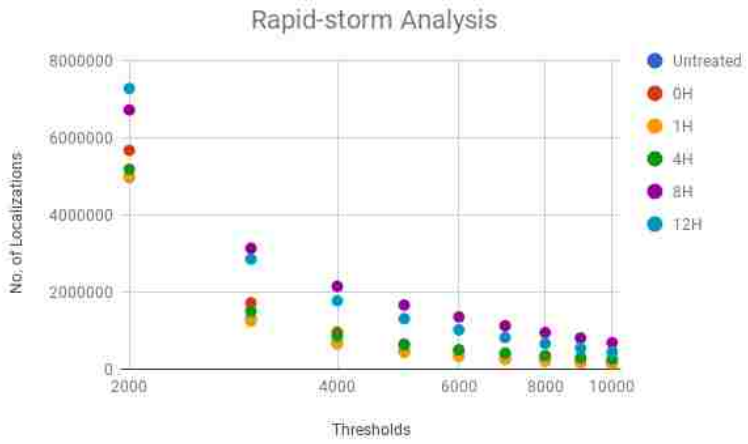

Figure 15. The localizations analyzed through Rapi*d*STORM run with thresholds limited between 2000 and 10,000.

2.3.3.3 Cleaning Data

Cleaning data is essential in super-resolution localization microscopy to guarantee a high spatial resolution, especially when the technique is used to visualize small cell organelle such as proteins (Wang et al., 2014). The output after the run of the Rapi*d*STORM is a table contains multiple columns and rows. The columns are presenting the x coordinate, y coordinate, frequency, amplitude and resolution, and each row correspond to detected spot (H-NS molecule). Each spot has different intensity, and the detected spots that are too dim or too bright were rejected based on the intensity threshold which was 50,000. In Figure 16-A, the blue detected spots (pixels) are the spots that were rejected in the cleaning step due to high the intensity output. This step is a standard step in the field of super-resolution fluorescence microscopy (Wolter et al., 2012a). Figure 16-B, is showing the localization after the imaged sample was cleaned, however, there were still blue spots next to every red spot. These before (blue) and after (red) detected spots are the drift in the localization that happened through the imaging. Therefore, the drift of the samples must be corrected. In our study, the drift which is the movement of the spots

from their localized place through frames was corrected after the acquisition. In Figure 16-B, the localizations that appeared in adjacent frames and within 10 nm to each other were regrouped as a single molecule which resulted in what is in Figure 16-C. We exploited a redundant cross-correlation method reported by Wang et al. to correct the drift (Wang et al., 2014). In Figure 16-D, the cleaned, drift-corrected spots were rendered to form the super-resolved images.

These steps of cleaning data were completed using a custom program, SRMC3, written in MATLAB (MathWorks, USA). Parameters were set for cleaning data as the following: the intensity was set as 50,000, the radius between two localized spots was set at less than 10 nm in order to be considered as one spot and the pixel size was 160 nm.

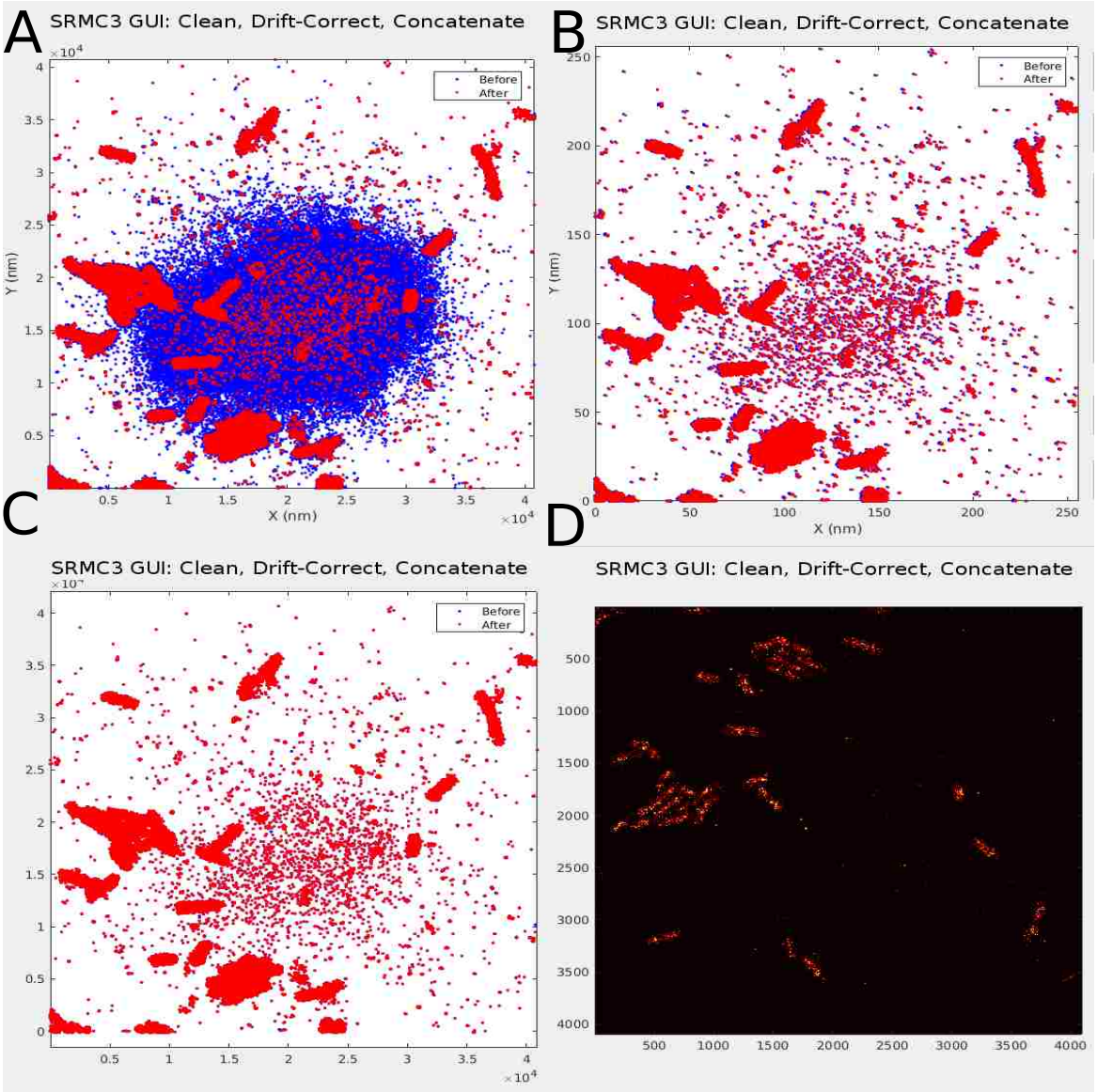

Figure 16. The steps of re-constructing the raw images into super-resolved images using Matlab. A, before cleaning, B, after cleaning, the maximum intensity was 50,000. C, after the drift-correction to sub-5 nm, the image size was 256 x 256 pixels, pixel size was 160 nm. D, after rendering the image into super-resolved image.

2.3.4 Super-Resolved Microscopy Analysis

2.3.4.1 Super-Resolved Images

After cleaning, drift-correcting and concatenating steps, super-resolved images were processed using ImageJ. The file of the clean, drift-corrected and concatenated image was

opened in ImageJ to set the color scale which was from 0 to 50. Then, the image was processed as a Red-Hot image and saved (Figure 17).

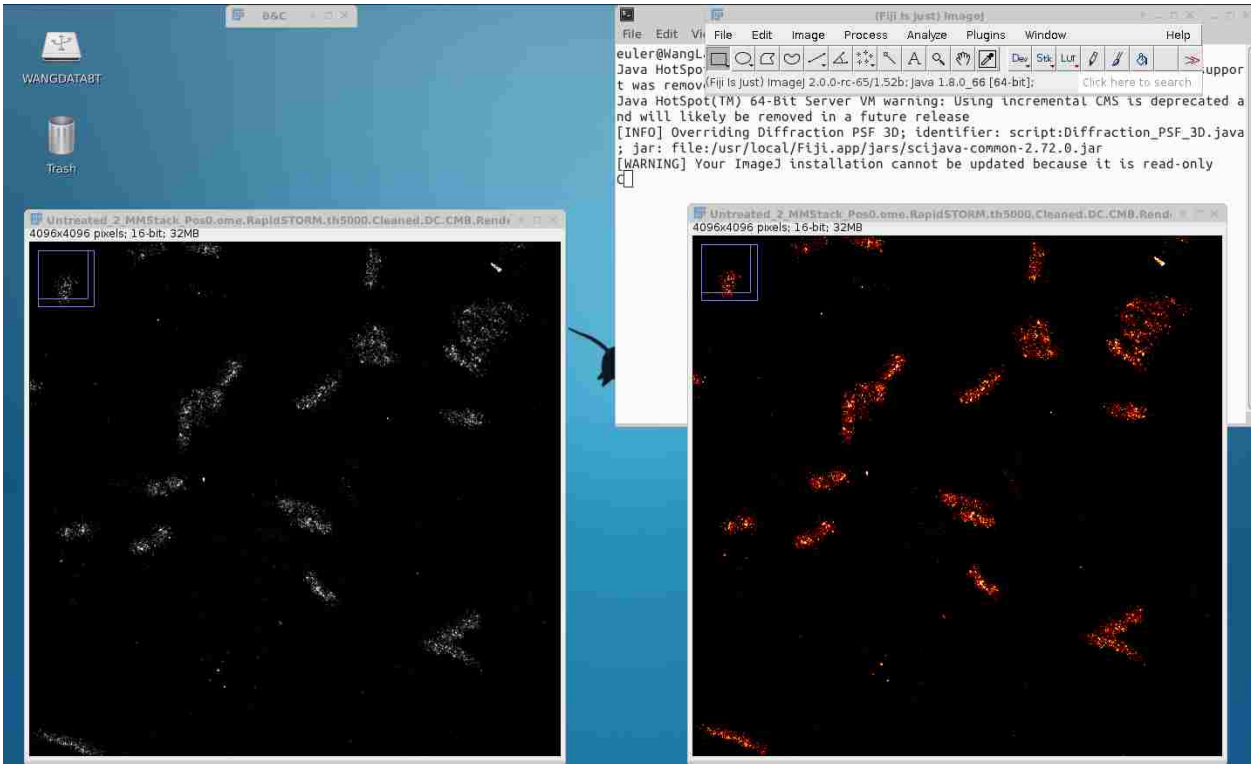

Figure 17. Screen-shot shows the two stages of transforming cleaned, drift-corrected and concatenated image (left) into Red Hot image (right) using ImageJ.

2.3.4.2 Statistical Analysis

2.3.4.2.1 Voronoi Diagrams

Mainly, the localizations of the molecules of H-NS proteins in *E. coli* were determined by using Voronoi diagram tessellation. Voronoi diagrams were used to understand the cumulative spatial distribution of the fluorescent H-NS proteins within the cells. First, H-NS proteins can form clusters that vary in the size, in the number of proteins molecules which will be forming the clusters, and in the density. The H-NS cluster is a group of H-NS proteins positioned closely together, and those clusters were observed under the super-resolved fluorescent microscopy. Voronoi is a technique of partitioning an area into multiple polygons based on “seeds” which are

the center points of each polygon. The main idea of having polygons drawn between the seeds which in this study are represented by H-NS molecules is to be able to measure the distance between each seed and its neighboring points. It is critical to understand that the bisectors are based on equal distances between the nearest two points or two seeds. For example, if there are two points placed near each other's, one line will be equally separating the distance between the two of them. If one seed or one point is added, the one line that was dividing the two points equally will be cut by another line which will be dividing the area around the three points equally (Figure 18) (Levet et al., 2015).

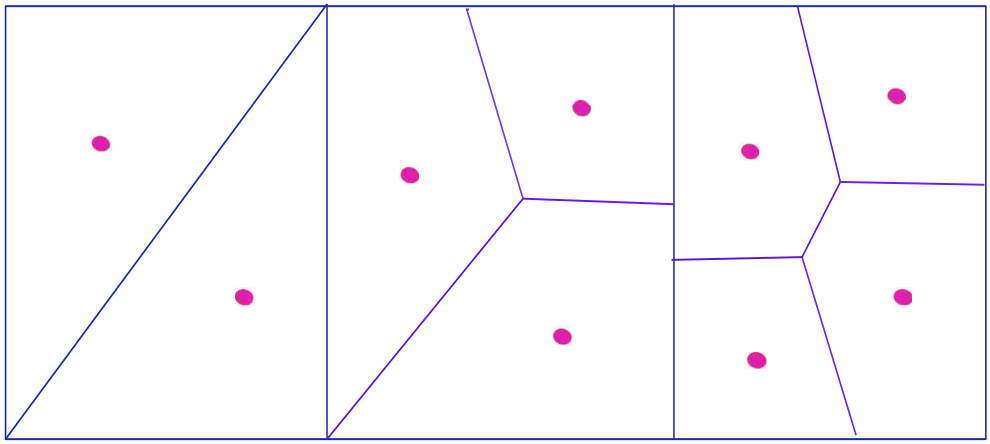

Figure 18. Illustration of the equal separation of the area based on the central point's

This equal separation of seeds by polygons will be repeated with every addition of new seeds or points (Levet et al., 2015). Each polygon will be surrounded by neighbors' polygons defined by their seeds within every polygon until polygons cover the full area of the cell (Figure 19). The segmentation of Voronoi will be based on the computed values of the spatial distance among H-NS proteins as points and among the neighboring H-NS proteins.

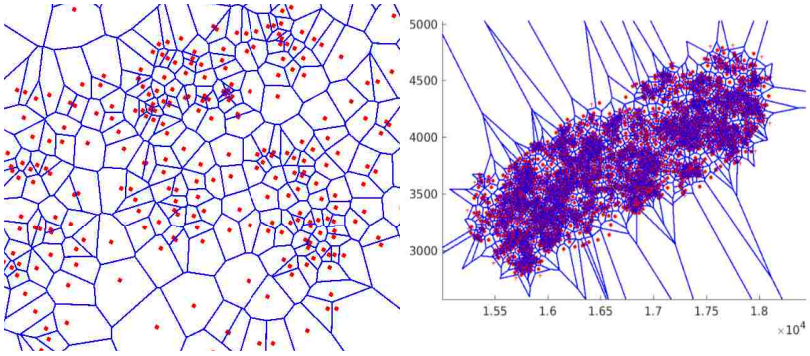

Fig 19. Left, an illustration of Voronoi diagram showing the seeds (Red dots) and the surrounding polygons (Blue lines). Right, an example of Voronoi application on *E. coli* cell.

2.3.4.2.2 H-NS Proteins' Molecular Parameters

By using the Voronoi segmentation method to segment and quantify localizations based on super-resolution microscopy data, multiple parameters were quantified and plotted (Levet et al., 2015). The Voronoi diagram divides the super-resolution image into multiple polygons based on centered localized molecules, and every polygon (p_i) of each seed (S_i) has an area that can be quantified and has multi-rank neighboring polygons. The first-rank of the surrounding neighboring polygons ($P_{i,j}^1$) of the seed (S_i) can be defined as n_i^1 polygons of area ($A_{i,j}^1$) which share the edges with the polygon (p_i). The polygon (p_i) is centered based on the seed ($S_{i,j}^1$) (Figure 20) (Levet et al., 2015).

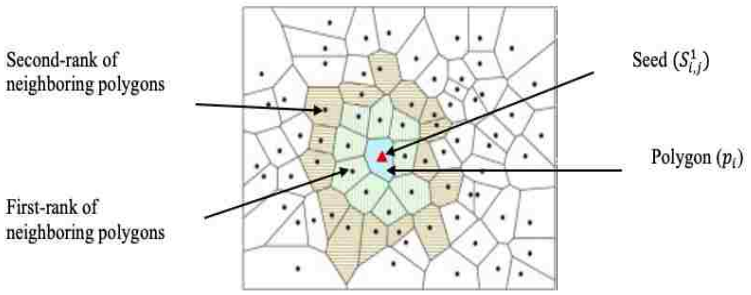

Figure 20. General scheme of the multi-rank neighboring polygons (Tu, Fang, Li, Shaw, & Chen, 2014).

Additionally, higher rank polygons ($P_{i,j}^{k}$), $K > 1$ can be determined as (n_i^k) polygons that share edges with ($P_{i,j}^{k-1}$). The neighboring polygons of seed (S_i) at the *K*th rank can be defined by the $\{n_i^1, \dots, n_i^k\}$ detected molecules. Accordingly, many parameters can be determined for each localized seed (S_i) such as the polygon area $\left(A_i^k\right)$, density and mean distance of seeds (Δ_{ave}). H-NS proteins' molecular area, density and mean distance were the main quantitative parameters for this research statistical analysis. With the previously mentioned parameters in Voronoi diagram, quantitative information about the seeds and the surrounding seeds with different molecular densities can be determined. The inter-molecule distances (d) were computed by using the following formula, where (x_i, y_i) and (x_j, y_j) are the x and y coordinates of the H-NS proteins molecules.

$$d(p_i, p_j) = \sqrt{(x_i - x_j)^2 + (y_i - y_j)^2}$$

The mean inter-neighbor distances between H-NS proteins molecules were calculated using the following formula:

$$\Delta_{ave}\,(p_i) = \frac{\sum_{p_j} d(p_i, p_j)}{N\ p_i}$$

- p_j is a neighbor of p_i, $i = 1, 2, \dots, n$.
- N_{pi} is the number of neighbors of p_i

The density of H-NS proteins was computed as follows:

$$p(p_i) = \frac{1 + N_{p_i}}{A_{p_i} + \sum_{p_j} A_{p_j}}$$

- p_j's are neighbors of p_i
- N_{pi} is the number of neighbors of p_i

- A_p's are the areas of polygonal areas occupied by protein $p(p = p_i \text{ or } p_j)$ (Levet et al., 2015).

The differences among the three calculated parameters distributions were tested by applying Kolmogorov-Smirnov (K-S) test. Kolmogorov-Smirnov test is a nonparametric hypothesis test that evaluates the difference between the cumulative distribution function (cds) of the distributions of samples. K-S test does not require the data to fall in normal distribution (Hassani & Silva, 2015). The test seeks to determine whether there exists a statistically significant difference between the distributions among the six plotted samples written in MATLAB (MathWorks, USA).

2.3.4.2.3 Clustering Identification Analysis of H-NS Proteins

Regions with higher molecular densities can be combined to smaller and denser polygons known as clusters (Levet et al., 2015). The cluster identification was based on identifying a density threshold to decide whether neighboring points can form clusters or not (Levet et al., 2015). Many methods have been utilized to analyze data localization attained using single-molecule localization microscopy; however, one of them has been reported to be the most efficient in statistically identifying cluster formations (Jiang, Park, Challapalli, Fei, & Wang, 2017). The pair-correlation method is an example of one of the methods that was applied to identify the presence of clusters, measure cluster density, and estimate the overall size of the clusters, but it cannot provide a precise number or localization of the molecules in each cluster (Sengupta & Lippincott-Schwartz, 2012). A limitation of another method that was used for quantitative analysis of clusters is the sensitivity towards background noise in density-based spatial clustering analysis with noise (DBSCAN) which allows the classification of particles in an image into clusters (Ester, Kriegel, & Xu, 1996). The SR-Tesseler based on Voronoi

diagraming was able to overcome the limitations in the previously mentioned methods, so it was used to identify cluster formations and behaviors in this research study. The cluster quantification analysis was based on the nearest neighbor distribution functions to be able to detect a cluster density (Jiang et al., 2017). Any molecules of H-NS proteins (p_i) reporting a local density above the assigned threshold (p_{th}) were selected along with its neighboring H-NS molecules to form a cluster. The threshold was selected based on the results of multiplying 2 by the average density of a chosen reference for a spatially uniform distribution:

$$p_{th} = 2 \times p_u$$

p_u is the average density for a spatially uniform distribution.

Chapter Three

3. Observations, Results, and Discussion

3.1 Synthesis and Characterization of Silver Nanoparticles

The properties of silver nanoparticles significantly impact their antimicrobial activities against bacterial cells. Therefore, many physicochemical characteristics have to be measured before utilizing AgNPs in experiments. The size of AgNPs in aqueous solutions and dried particles, average shape, surface charge, accumulation, and dispersity are the main characteristics that were determined for the silver nanoparticles in this study. The characterization process to ensure the functionality of the synthesis nanoparticles included multiple techniques such as UV-vis spectroscopy, transmission electron microscopy (TEM), dynamic light scattering (DLS), and flame atomic absorption spectroscopy (AAS).

The absorbance spectra measured by UV-vis spectroscopy revealed a peak at λ max = 416 nm (Figure 21). The peak was present for both PVP-AgNPs and PEI-AgNPs. On the other hand, several differences were observed. First, the major peak in the spectrum of the PEI-AgNPs possessed a shoulder to the right of 416 nm with a weak but broad band which centered at ~495 nm, possibly due to a small amount of particle aggregation.

The structure of the nano-cube shape was observed under the transmission electron microscopy (TEM), and the diameter size was determined. The average size of the silver nanoparticles was 33.5 ± 6 nm in both PEI-AgNPs and PVP-AgNPs (Figure 22). The diameter was measured by using the software ImageJ.

The shape of PVP-AgNPs and PEI-AgNPs in TEM images were mostly cubical shape with sharp edges (Figure 22). However, aggregates of nanoparticles were observed for the PEI-AgNPs. In addition, other shapes such as triangular and rounded nanoparticles were seen. The

morphological change in PEI-AgNPs agrees with the observed shoulder in the UV-Vis spectrum at the wavelength of ~ 495 nm.

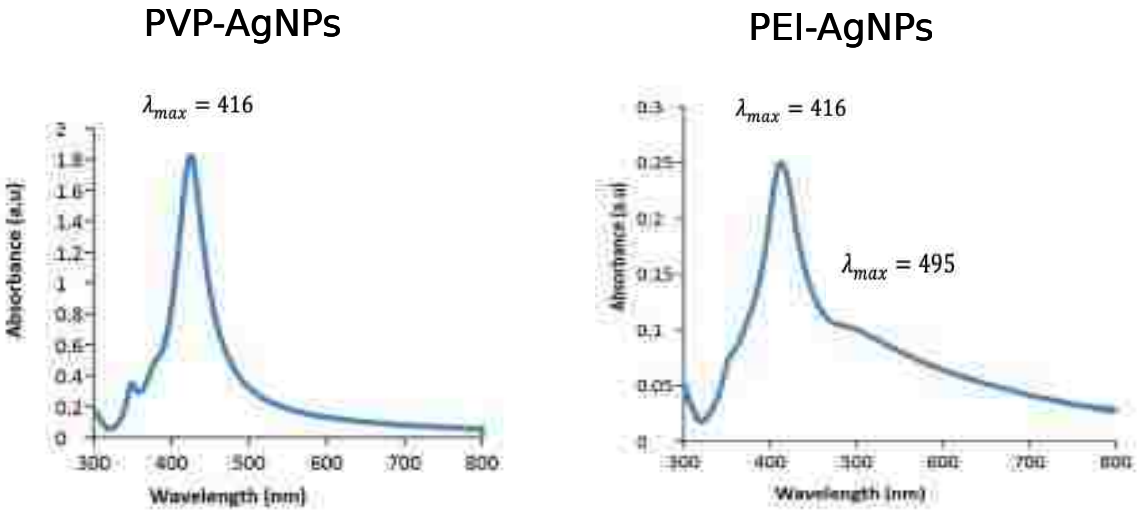

Figure 21. The wavelength of the nanoparticles (λ max = 416 nm)

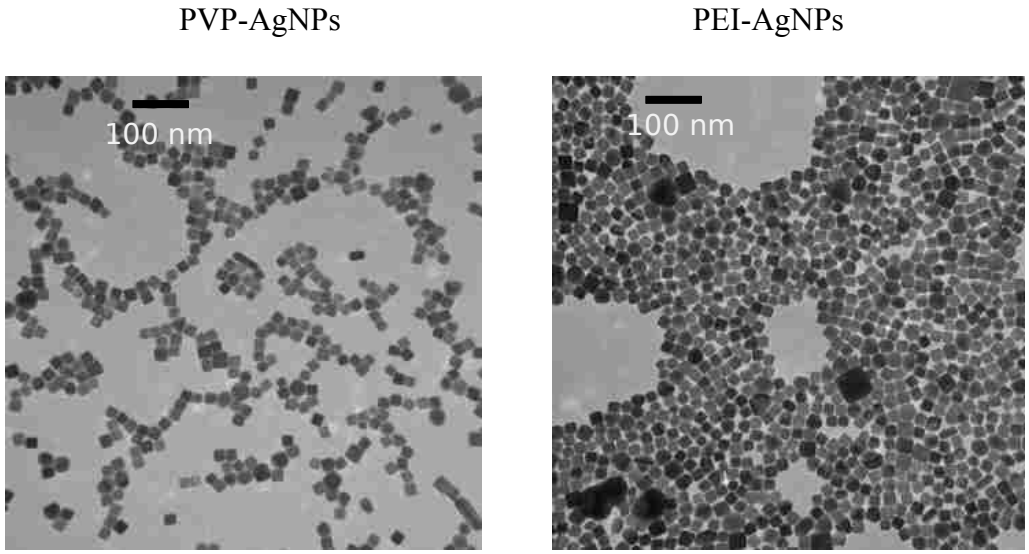

Figure 22. Transmission electron microscopy (TEM) images are showing the shape of the silver nanoparticles (diameter 33.5 ± 6 nm). The PVP-AgNPs are shown on the left (cubical) and the population of mixed shapes PEI-AgNPs are shown on the right (spherical, triangular, and cubical).

Dynamic Light Scattering (DLS) was used to analyze the hydrodynamic diameter and the

polydispersity index (PDI) of the nanoparticles in the aqueous solution. A particle's hydrodynamic diameter is the measurement of the behavior of particles in solution and the hypothetical distance between the core of the particles and the surrounded hydration layers. Once a dispersed particle moves through a liquid medium, a thin electric dipole layer of the solvent adheres to its surface. This layer influences the movement of the particle in the medium. Thus, the hydrodynamic diameter provides information about the NPs core along with any coating material and the solvent layer attached to the particle as it moves under the influence of Brownian motion (Malvern , 2011). The hydrodynamic diameter of the nanoparticles was 112.2 nm on average for the PVP-AgNPs. On the other hand, PEI-AgNPs hydrodynamic effective diameter was 162.3 nm and this increase might be due to the particle aggregation (Figure 23).

The polydispersity index (PDI) is an indication of the uniformity of AgNPs samples and the higher the index, the less disperse the sample is (Ardani et al., 2017). Generally, dispersed NPs are more toxic and active more than the NPs that are aggregated in large clumps, regardless of the nature of NPs (Liu et al., 2009). The polydispersity index (PDI) was within the range (0.05 – 0.7), and it was measured to be ~0.2 for PVP-AgNPs and PEI-AgNPs (Figure 23) (Danaei et al., 2018).

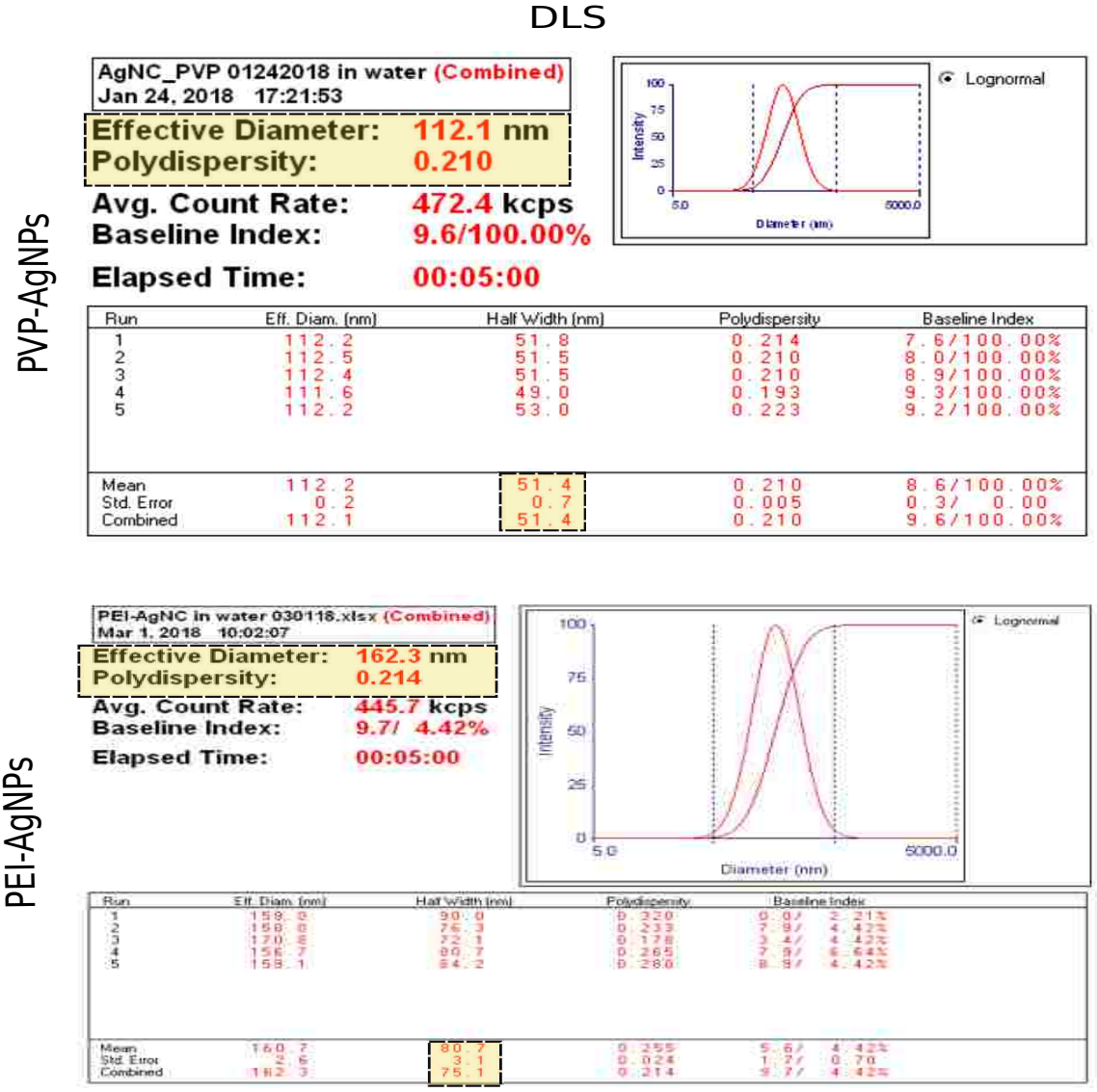

Figure 23. Dynamic Light Scattering (DLS) measurements result for the hydrodynamic diameter (see highlighted areas)

For the surface charges measurements, we determined the zeta-potential values as analyzed using atomic absorption spectroscopy (AAS). The PVP-capped AgNPs had a highly negative zeta potential of -39.44 mV ± 1.37 mV, which agrees with the literature (Haider & Mehdi, 2014). On the other hand, the PEI-capped AgNPs attained zeta potential of +19.19 mV ± 1.80 mV, indicative of a positively charged surface and thus a successful ligand-exchange (Figure 24). The mass concentration was determined to be 1.5 mg/ml.

Zeta Potential

PVP-AgNPs

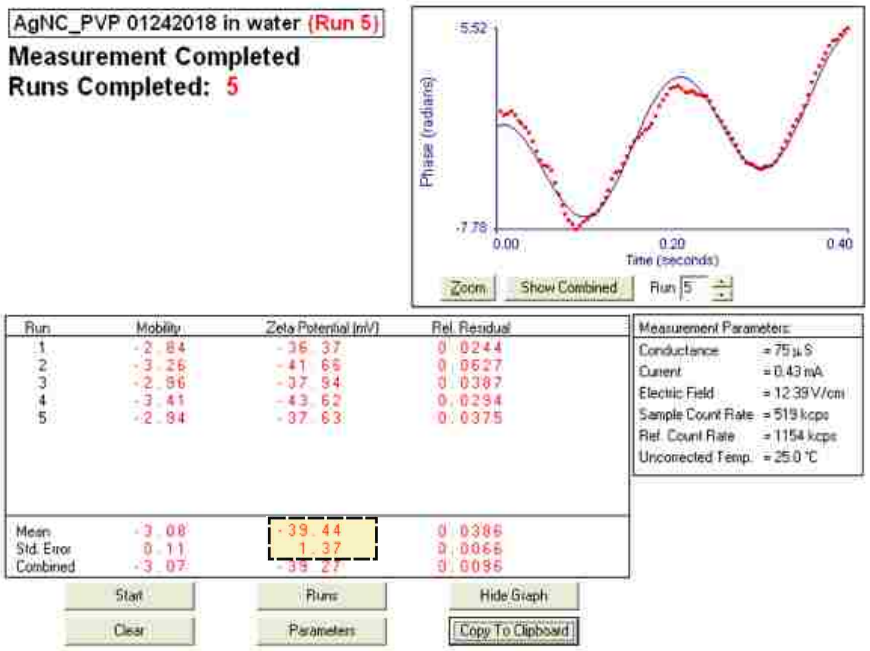

PEI-AgNPs

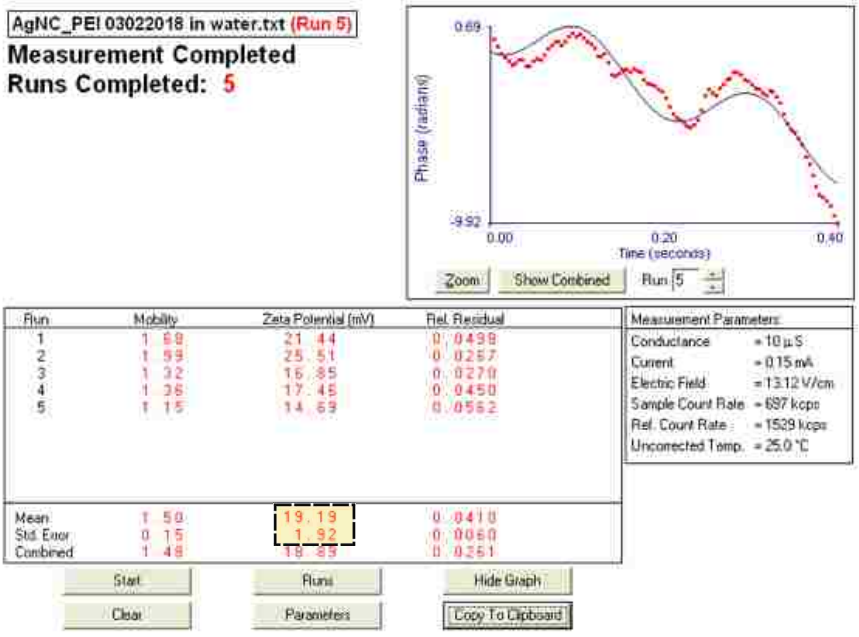

Figure 24. Zeta potential analysis result illustrating the coating charges on both synthesized NPs (highlighted areas)

The stability of AgNPs was tested to understand the changes on the hydrodynamic diameter over time in bacterial growth medium M9GTC. The average hydrodynamic diameter of AgNPs changed as well as the polydispersity after 24 hours of incubation in bacterial growth medium M9GTC (Figure 25). The mean hydrodynamic diameter of PVP-AgNPs after 24 hours of incubation at 37 ºC with shaking at 250 rpm increased from 130.4 nm to 279.4 nm, which is an indication of the increase in the accumulation of silver nanoparticles and the polydispersity changed. The PEI-AgNPs showed opposite results, where the effective diameter decreased from 575.9 nm to 409.4 nm, indicating that PEI-AgNPs behavior in M9GTC is not stable due to the coated material. The polydispersity decreased as well for PEI-AgNPs in M9GTC media after 24 hours of incubation (Figure 25, highlighted area). However, the UV-vis absorption did not show a significant difference between AgNPs incubated for 24 hours compared to the control samples. The diameter size measured by TEM images is for the dried particles, which may contribute to the difference in results.

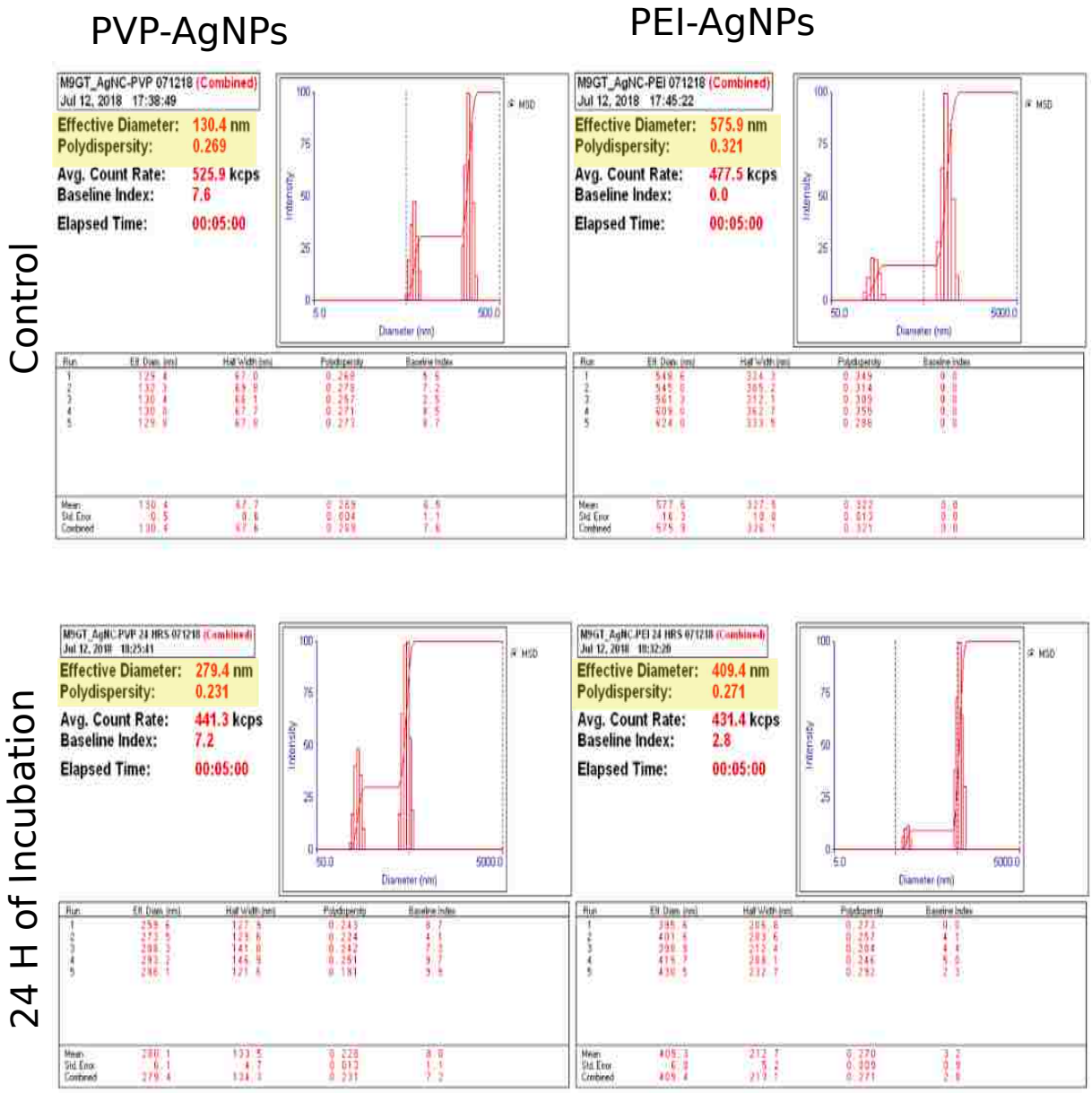

Figure 25: Dynamic Light Scattering (DLS) analysis for PVP-AgNPs and PEI-AgNPs

3.2 Release of Silver Ions into Solutions

Previous reports in the literature showed that the release of silver ions (Ag^+) from silver nanoparticles plays an important role in the antimicrobial activities and mechanism of AgNPs. Therefore, the action mechanism of silver nanoparticles depends on the concentration of released

silver ions into the media. It has been proposed that silver ions might demonstrate a greater effect on bacteria cells than silver nanoparticles, especially NPs with diameter size larger than 15 nm (Kędziora et al., 2018). Therefore, the released concentration of Ag^+ was measured. The concentration of released ions from the two types of AgNPs is shown in Table 1, and ranged between 5.15 µg/L and 25.5 µg/L in M9GTC medium only without any bacterial presence in the medium. The low concentrations of Ag^+ ions in M9GTC in comparison to the Ag^+ ions in water are because of the presence of Cl^- in the M9GTC medium, which is likely for both ions to interact to form AgCl in the solution (Badawy et al., 2010). Based on a previous study from our lab (Haque et al., 2017a), silver ions at these concentrations are unlikely to be playing the major role of effecting the bacterial cells; however, it is supposed to be contributing to the antibacterial activity of AgNPs.

Table 1. The Ag^+ concertation's measured using AAS

Measured Samples	**Concentration µg/L**
PVP_AgNPs in M9GTC	25.5 µg/L
PEI_AgNPs in M9GTC	5.15 µg/L
PEI_AgNPs in distilled water	91.3 µg/L
PVP_AgNPs in distilled water	238.97 µg/L
PVP_AgNPs from stock solution 1.2 mg/ml	1143.119 µg/L
PEI_AgNPs from stock solution 1.5 mg/ml	298.104 µg/L

3.3 Bright Field Imaging

Using bright field microscopy, morphological changes in *E. coli* bacteria in the presence of AgNPs were observed. The bright field images showed that the treated bacteria were shorter than the untreated cells. The treatment of 40 µg/ml of PVP-AgNPs and PEI-AgNPs affected the cells' lengths during the experimental incubation time. After 1 hour of incubating bacteria with AgNPs, antibacterial properties of the AgNPs affected the cells' sizes dramatically. In both treatments types of AgNPs, the cells size at 0h and 1h did not decrease in the length and was equivalent to the control (untreated cells). However, from 1 to 4 hr, the cells entered a suppression period where the cells shrunk (Figure 26). Previously, it was observed that upon exposure to silver nanoparticles, *E. coli* cells entered a stress period and converted to shorter cells (Lok et al., 2006). In Figure 37, the control (C) image depicts the untreated cells (negative control) while the 0H image depicts treated cells at time zero of incubation (positive control). The 1H image present cells after 1 hour of growth in the presence of AgNPs, and subsequent images show cells after 4 hours, 8 hours and 12 hours of incubation. Cell size shrank at 4, 8 and 12 hr of incubation. These results are consistent with previous studies which have shown shrinkage and deformation in the bacterial cell due to the treatment of AgNPs and the released Ag^+ ions (Phanjom & Ahmed, 2017). It was observed that at 12 hours of treating cells with AgNPs, around 20% of the cells were able to grow back to their normal length. Previous study has shown that after 12 hours of suppression, *E. coli* were able to grow again (Haque et al., 2017b). The observed changes in the morphology of *E. coli* cells in term of the size shrinking might be because of an increase of the permeability of *E. coli* cell membrane resulting in some leakage of cell contents (Carlson et al., 2008).

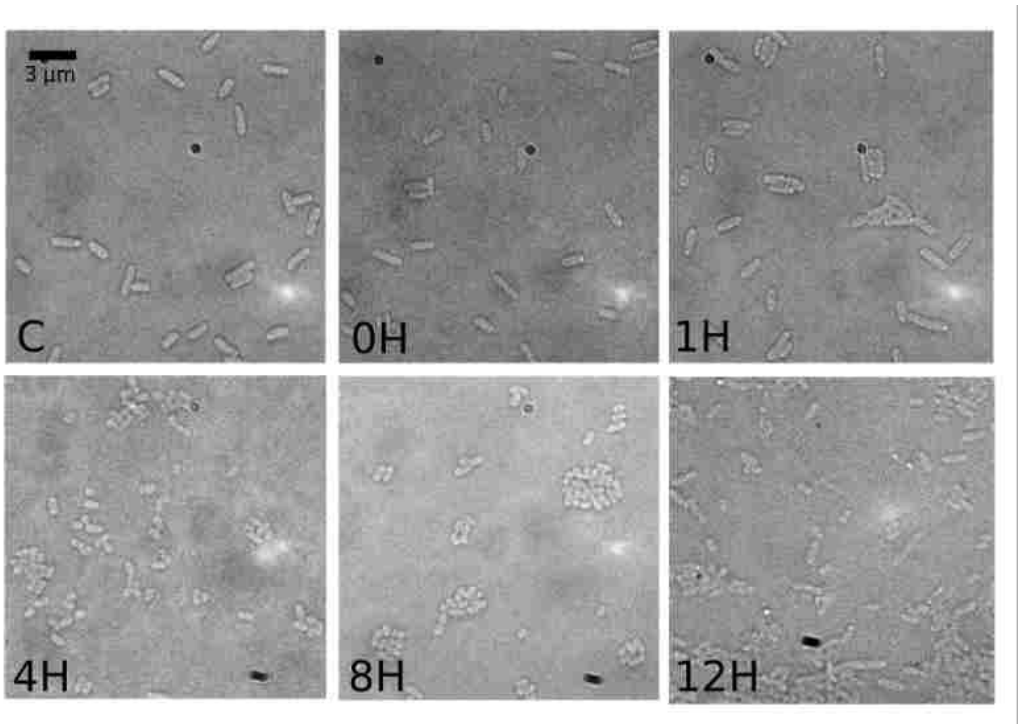

Figure 26. Bright field images were taking for fixed cells immobilized on a 3% agarose pad showing cell shrinkage with treatment time. Treatment time: C, untreated cells. 0H, treated cell but fixed immediately after the addition of AgNPs. 1H, cells treated for 1 hour then fixed. 4H, cells treated for 4 hours then fixed. 8H, cells treated for 8 hours then fixed. 12H, the maximum treatment time with AgNPs.

The ability of AgNPs to attach to the cell membrane and form large accumulations has been shown to shrink the cells (Chen & Bothun, 2014). Silver nanoparticle accumulations on cell membranes were observed in one of the experiments that was done without performing the centrifugation step (Figure 27). It was observed that AgNPs caused deformation in the *E. coli* bacterial cell membrane, likely driven by intermolecular and surface forces which can lead to lipid restructuring and local deformation (Chen & Bothun, 2014). During the imaging, few AgNPs were attached to the membrane of the cell due to the centrifugation step that likely separated AgNPs from cells and forced AgNPs to the bottom of the microcentrifuge tube (Figure 11, Left image).

Figure 27. Bright field image taken from a sample which was not centrifuged illustrating how AgNPs can be accumulated and attached to cells' membrane (as shown by the arrow).

3.4 Measurement of Cell Length

The cell lengths decreased to less than half the cells' length after more than 1 hour of treatment. Both PVP-AgNPs and PEI-AgNPs at 4 hours of treatment shrank the length of the cell to aprroximately 10 pixels, which may coincide with cells experiencing a suppressive period after 1 hour of incubation with AgNPs. Similarly, at 8 and 12 hours of treatment, the average decreased to less than 50% of the untreated cells, where the average length of the bacteria was 7 pixels and 9.9 pixels, respectively, for bacteria treated with PEI-AgNPs. The untreated, 0H, and 1H average cell lengths were 17 pixels, 14 pixels, and 18 pixels. respectively. Similarly, the cells treated with PVP-AgNPs were reduced in cell length similar to the cells treated with PEI-AgNPs. The average length of cells at 4H, 8H, and 12H were 10 pixels, 9 pixels, and 10 pixels, respectively. ANOVA showed that difference does exist among the treated samples which were treated at different times since the p-values for both PVP-AgNPs and PEI-AgNPs were less than the significance level. The calculated p-values for both treatment types with PEI-AgNPs and PVP-AgNPs were <0.00001, and the cell's length results are significant at $p < 0.05$. The Measured cell lengths are shown in Figures 28 and 29 for PEI-AgNPs and PVP-AgNPs,

respectively. The number (n) of cells in each sample was 100, and data in Figures 28 and 29 are plotted in a box plot depicting the median, upper quartile and lower quartile of the cells, maximum, and minimum.

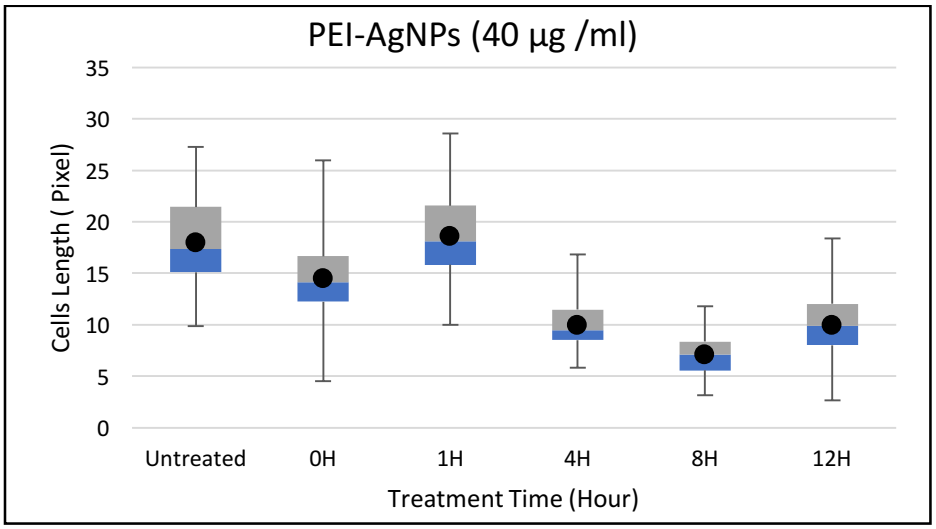

Figure 28. *E. coli* cell lengths differences in the absence and presence of 40 µg/ml of PEI-AgNPs incubated for up to a total of 12 hours, n=100 cells. The p-value is <0.00001.

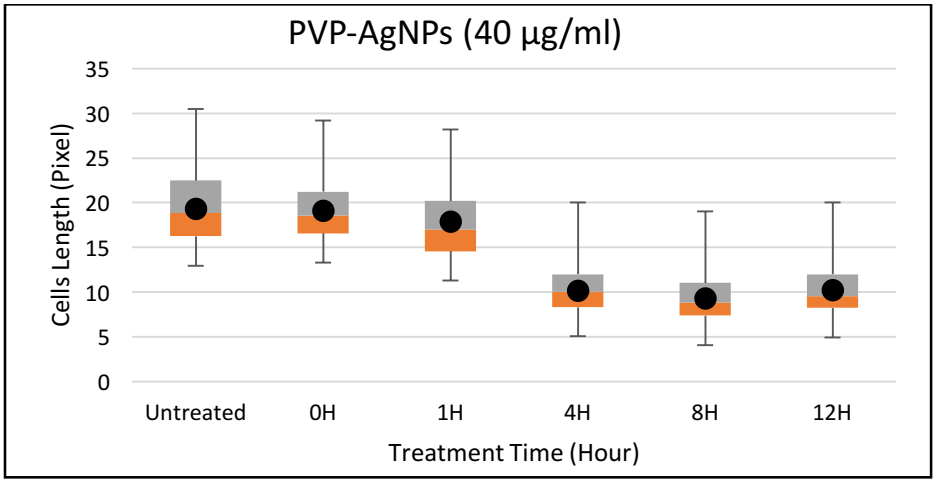

Figure 29. *E. coli* cell lengths differences in the absence and presence of 40 µg/ml of PVP-AgNPs incubated for up to a total of 12 hours, n=100 cells. The p-value is <0.00001.

3.5 Results of Super-Resolved Fluorescence Microscopy Imaging

3.5.1 Super-Resolved Images

Super-resolved images allowed us to have a look at the spatial distribution of H-NS proteins in *E. coli*. It was observed that H-NS proteins over the time of treatment increased cluster formation. Moreover, the H-NS proteins tend to center in the middle of the cells as shown in Figure 30. When treated with AgNPs for 12 hours, the proteins condense and form high-intensity clusters in the middle of the cell. Both sets of cells treated with PVP-AgNPs and PEI-AgNPs showed accumulation of H-NS proteins after 12 hours of treatment; however, there were differences observed in the intensity of the clustering between treatments.

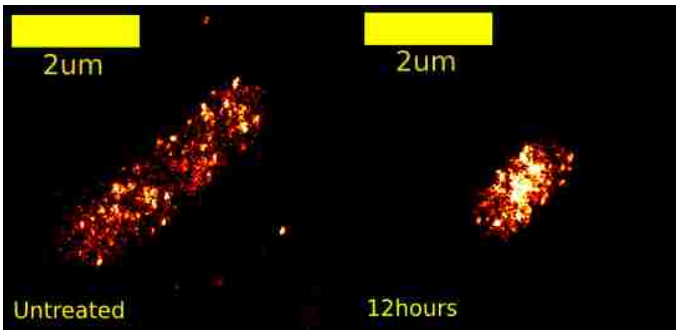

Figure 30. Super-resolved Fluorescence Images, where the image on the right depicts the distribution of H-NS spread throughout the cell in the absence of AgNPs and the image on the left depicts large clusters at the midpoint of the cell in the presence of AgNPs.

The accumulations of the clusters of H-NS proteins increased with the duration of incubation with silver nanoparticles (PVP and PEI). The changes in the formation of H-NS protein molecules became apparent at the following treatment times: 4, 8, and 12 hours for both AgNPs. The density of the clusters appeared to increase in the super-resolved images. The clustering of H-NS protein accumulated slowly from the first hour of AgNPs treatment and became more intense at 8 and 12 hours of incubation with AgNPs.

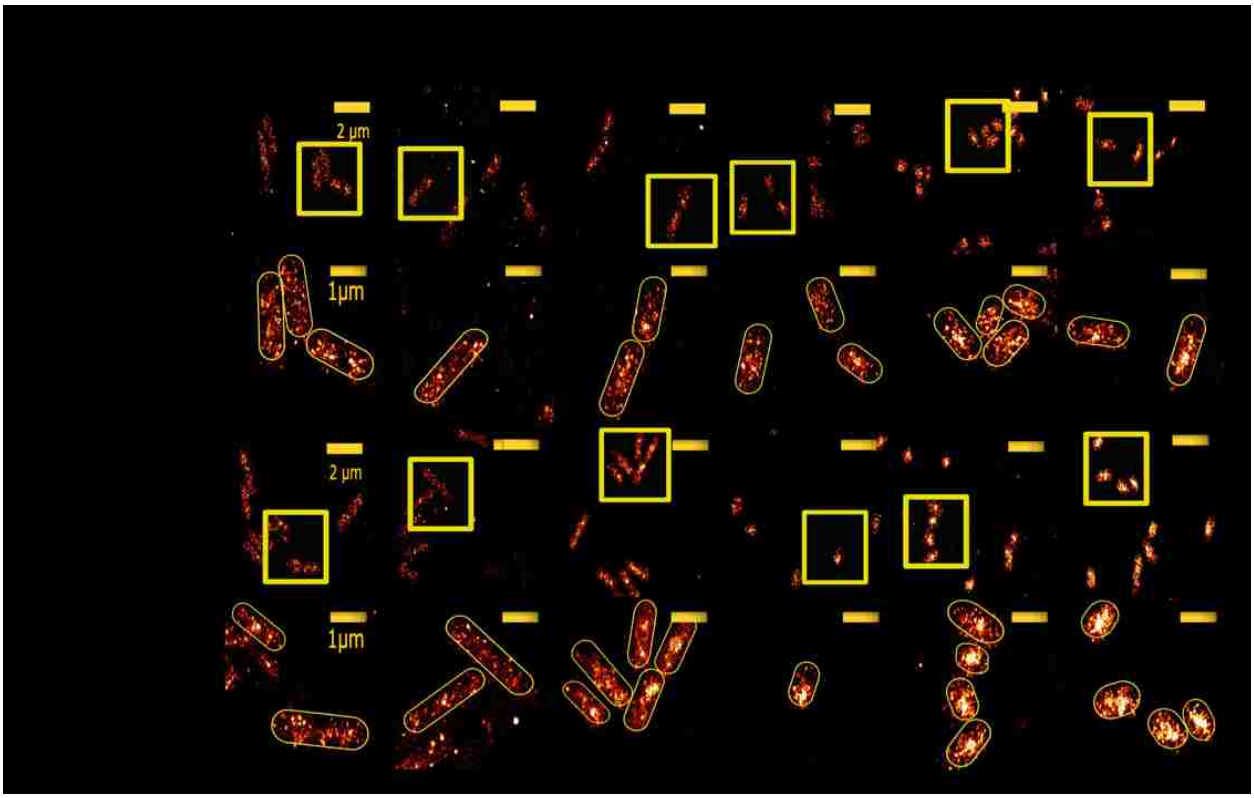

Figure 31. Reorganization of histone-like nucleoid structuring (H-NS) proteins in *E. coli* bacteria caused by AgNPs, revealed by super-resolution fluorescence microscopy. Top row shows the six incubation times for samples that were treated with PVP-NPs. Second row shows a zoomed-in image of the cells and the clustering. The third row shows H-NS clusters and cells incubated with PEI-AgNPs. The bottom row shows individual cells forming high intensity of clusters with increased incubation time. The replicate number was 100 to 300 cells per each sample.

3.5.2 Voronoi tessellation of H-NS proteins inside *E. coli*

Voronoi tessellation is the division of space into regions based on distance to points in a specific subset of the space (Levet et al., 2015). Utilizing Voronoi diagram segmentation, it was observed that H-NS proteins were centrally packed after 12 hours of treatment. In Figure 32, the top three images show the segmentation of the polygons for the proteins seeds (red dots) and the density of the cluster formations. In the untreated cell, the clusters were more dispersed throughout the cell volume, while in PVP-AgNP and PEI-AgNP-treated cells, the formation of

the clusters increased significantly, increasing the density. The bottom images show a zoomed-in depiction of polygons drawn based on the aggregation of the H-NS proteins and the consequent overcrowding of H-NS proteins in the 12 hours samples.

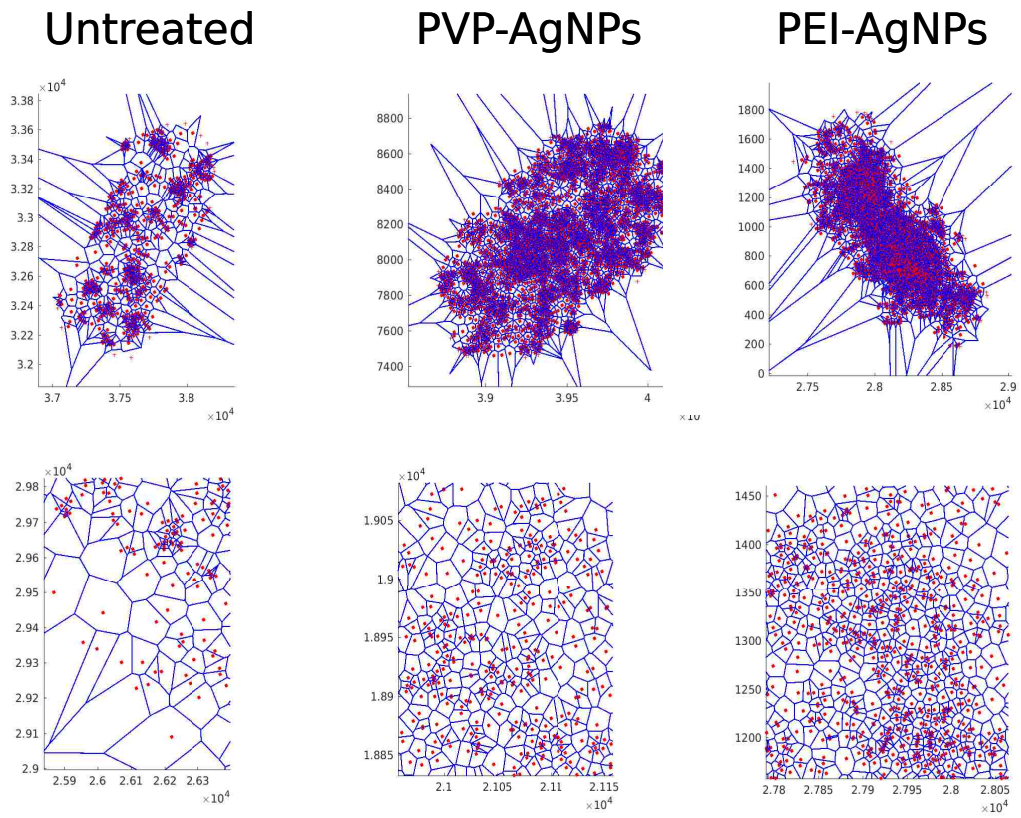

Figure 32. Voronoi diagram is showing the entire cell with the polygons at the top. The bottom three images show zoom in on the localization of the H-NS points.

3.5.3 Quantification of H-NS Protein Molecular Localizations

H-NS Proteins' Molecular Area

The molecular area of H-NS proteins can be defined as the occupied area (polygon) by one H-NS molecule in Voronoi segmentation (Levet et al., 2015). The decrease in quantified H-NS protein molecular area indicates a change in the spatial organization of the H-NS protein. In Figure 33, the molecular areas occupied by H-NS proteins decreased over the 12 hours of treatment. Figure 33. shows log-normal distribution of the calculated values of the molecular

area occupied by the H-NS proteins based on their defined x and y coordinate. The peaks of the distributions shifted to the left, indicating that the molecular area decreased. Similar changes in the distribution were observed at 8 hours and 12 hours; however, 8 hours treatment with PVP-AgNPs showed higher frequency. The increase in the peak shifted to the left of 8 hours of PVP-AgNPs treatment is explained by the cells number which was the highest among the cell numbers in the other treated samples.

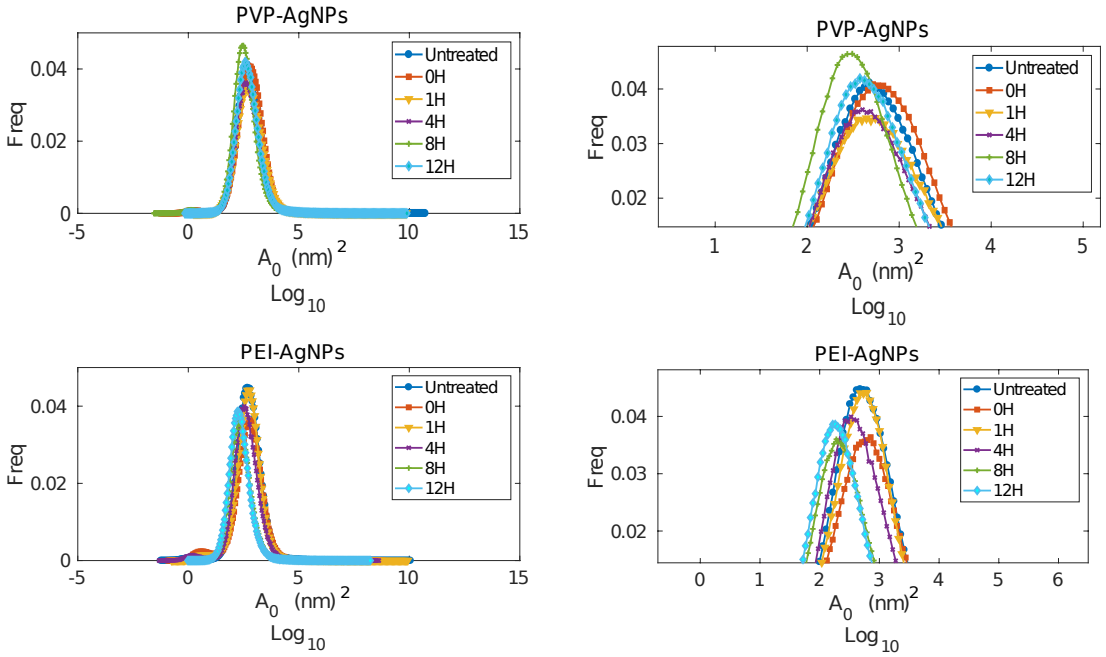

Figure 33. H-NS protein molecular area log-normal distribution. Left, distribution of the quantified H-NS molecules occupied area for the six treated samples. Right, zoom-in look showing the shift in peaks toward the left, n=100-300 cells. The p-value is <0.00001

The Average Distance between H-NS Proteins Molecules

The average distance between H-NS proteins is the inter-molecule distance between neighboring H-NS proteins. The average distance between H-NS proteins molecules decreased upon the treatment time. The decrease in the distance between each H-NS molecule and its neighboring molecules is shown in the shift of the distribution of frequency of samples throughout the treatment time. Both PVP-AgNPs and PEI-AgNPs shifted inter-molecule distance

to smaller distances in the treated samples at 8 and 12 hours of incubation. Similar results were observed in the average inter-molecule distance between treated cells throughout the treatment incubation time (Figure 34)

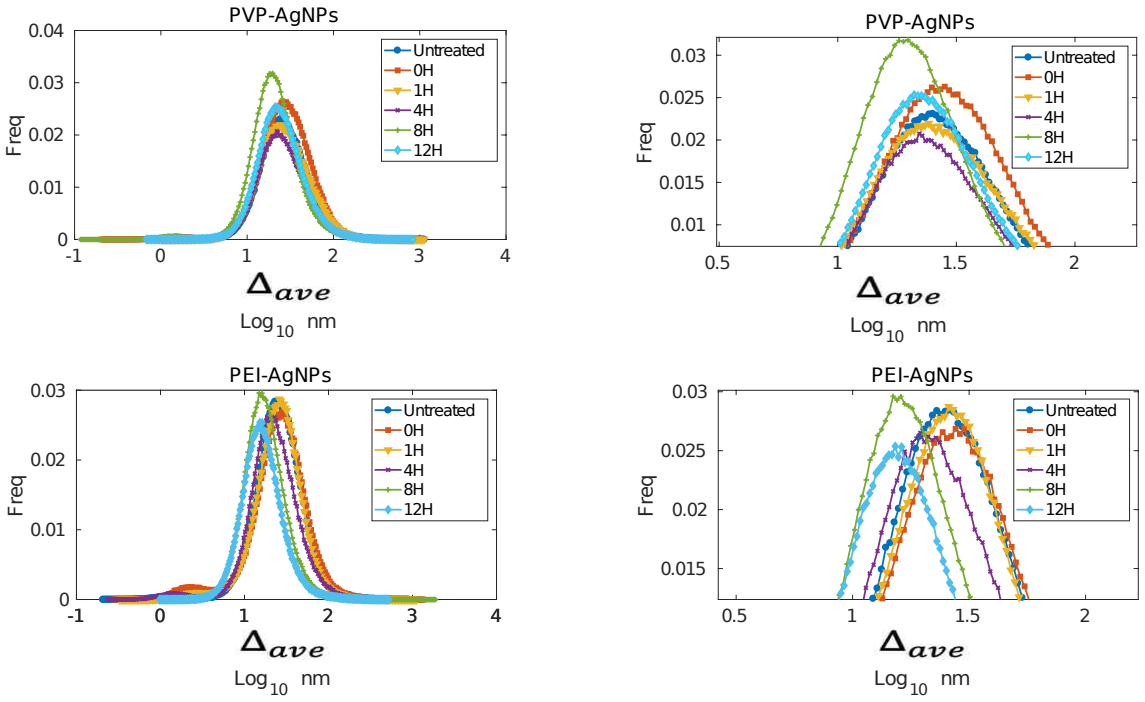

Figure 34. log-normal distribution results of measuring the inner-distance between neighboring H-NS proteins molecules among the treatment time. left column of graphs is showing the full distribution result of PVP-AgNPs and PEI-AgNPs. Right column, is showing a zoom in to the shifted peaks to left indicating a decrease in the inter-molecule distance between neighboring H-NS molecules, n=100-300 cells. The p-value is <0.00001

H-NS Protein Molecular Density

With the decrease in the molecular area and the inter-distance, the molecular density of the H-NS protein increased. The molecular density was measured as number of proteins divided by the sum of the identified occupied area (see equation under method section). The peaks of the log-normal distribution of the treated samples with AgNPs shifted right indicating an increase in the clustering density (Figure 35). Both PVP-AgNPs and PEI-AgNPs caused an increase in the density of H-NS molecules with the greatest effect observed after incubation for 8 and 12 hour.

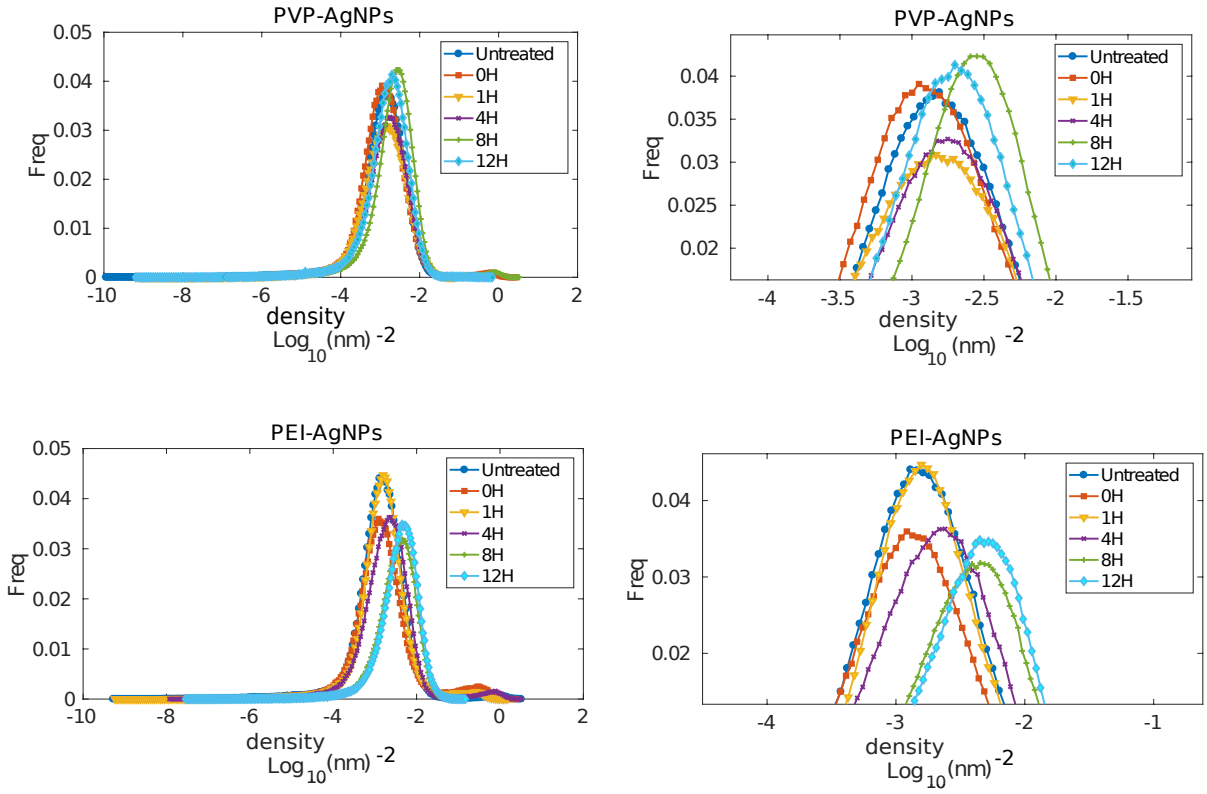

Figure 35. H-NS protein molecular density log-normal distribution. The shift in the distribution of the samples to the right is indicating an increase in the density of the H-NS molecular density at the following treatment time 4H, 8H and 12H, n=100-300 cells. The p-value is <0.00001

3.5.4 H-NS Protein Cluster Identification

The cluster identification of H-NS protein showed variation among treatments. The untreated cells did not show large numbers of cluster formations (Figure 36 top images), while the treated cells after 12 hours showed numerous large formations of clusters (Figure 36 bottom images).

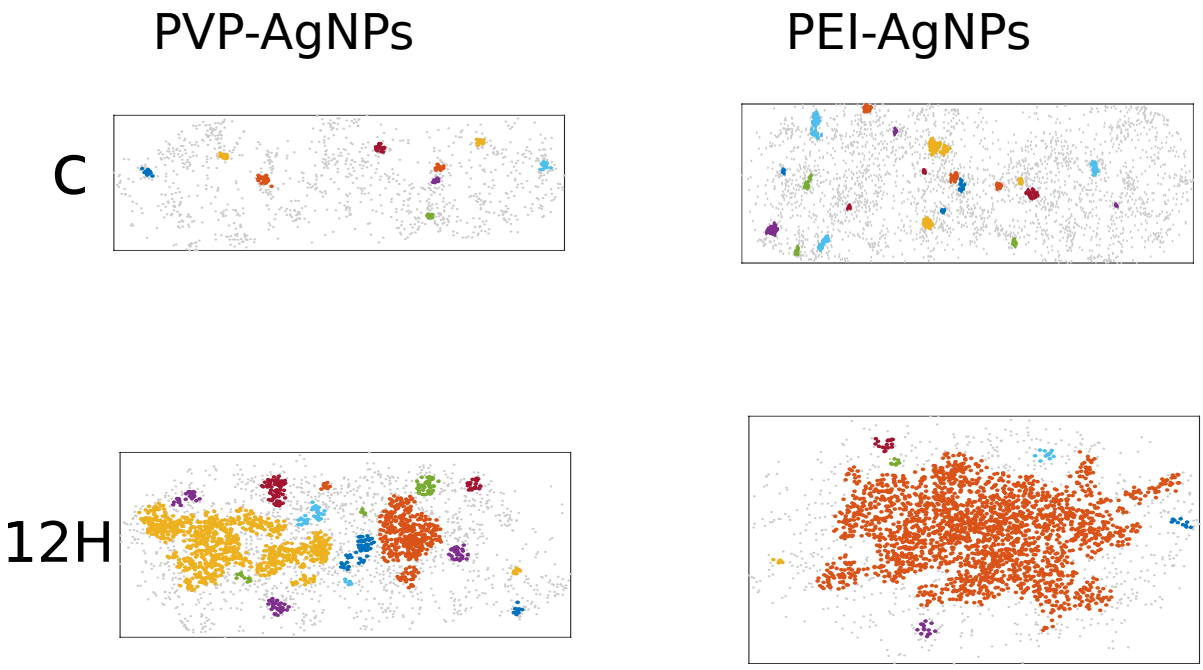

Figure 36. An illustration in colors of the variety of cluster density formations among samples. Gray dots are single localized H-NS proteins, while colored dots are H-NS proteins forming clusters.

The localization of H-NS protein is represented by the gray dots, while the colored regions represent clusters. In the negative control (i.e. untreated cells), the H-NS proteins were dispersed throughout the cytoplasm of the cell. Only small clusters were observed. The largest formation of clusters occurred in the samples treated for 12 hours with AgNPs. In Figure 37, the bottom images show clusters highlighted in different colors. Both images shown in the bottom row were treated with AgNPs for 12 hours. The bottom left image shows large groups of clusters in the treatment with PVP-AgNPs. The bottom right image shows more extensive formation of clusters in the treatment containing the PEI-AgNPs.

3.6 Discussions

The role of silver nanoparticles to effect bacterial cells has been investigated in this study using a different method. Quantitative super-resolution fluorescence microscopy was used to

study the response of bacteria to treatment with AgNP by looking at the spatial reorganization of the H-NS proteins. The diameter size of the used AgNPs (33.5 ± 6 nm) makes it difficult for NPs to penetrate the cells' membranes unless the AgNPs were broken down into small particles, which was unlikely to occur in our results; however, small NPs were reported inside the cells (Morones et al., 2005). Previous work reported that small NPs with a larger surface-to-volume ratio had a greater effect on the same *E. coli* strain compare to larger NPs (Baker et al., 2005). In our work, the release of silver ions is controlled by the surface ligands of the used AgNPs (Long et al., 2017). The dissolution rate and the number of silver ions from polyvinylpyrrolidone-stabilized AgNPs are proposed to be higher in the media than those branched polyethylenimine-capped AgNPs with positive charges (Long et al., 2017). Having AgNPs capped with positive charges makes Ag^+ ions released more and be absorbed on the membrane of gram-negative bacteria than negatively charged AgNPs or neutral coated AgNPs (Danaei et al., 2018). Suggesting that the released silver ions can interfere with the negatively charged cell membrane bacterial cells; moreover, the intracellular silver ions can directly bind with the thiol-containing enzymes (Long et al., 2017). Therefore, measuring the concentration of the released Ag^+ ions in the presence of the bacterial growth might be inaccurate due to the susceptibility of cells to uptake the silver ions.

As previous studies have shown several mechanisms of bacterial damage caused by AgNPs, including DNA condensation caused by AgNPs and Ag^+ ions using transmission electron microscopy (Feng et al., 2000). Compared to the condensation of DNA, which has been observed for bacteria exposed to AgNPs and Ag^+ ions, the changes in the spatial distribution and organization of proteins have not been reported due to the lack of the required specificity and spatial resolution. In our study, H-NS proteins reorganization caused by the treatment of AgNPs

might be explaining the previous observation of DNA condensation which suggests that the DNA condensation is happening because of the effect of the resealed silver ions on the DNA binding proteins. The aggregation of H-NS clusters in the middle of the cells as the time of treatment increases might prevent DNA from unwinding. The DNA condensation might be an obstacle for the cell to express genes for survival purposes or growth (Wang et al., 2011). The results of the increase of clusters formation at 8 and 12 hours caused by both AgNPs might be preventing genes regulation because of the substantial folding and condensation of the bacterial DNA (Wang et al., 2011). Also, many studies have reported the average behavior of many bacteria responding to AgNPs and Ag^+ ions in terms of antibacterial activity on the growth rate and on the proteins expression levels (Kędziora et al., 2018). However, although single-molecule imaging has been drawing extensive attention, little progress has been made to study the changes on the spatial localization of major DNA binding proteins caused by AgNPs.

Even though it was observed that treating *E. coli* cells with AgNPs up to 12 hours have caused shrinkage, it was observed that cells were able to grow back to their normal cell size after 12 hours. Previous study has shown that *E. coli* cells after 12 hours of treatment can grow to the normal growth rate and this bouncing back might suggest the possibilities of bacterial adaptation to AgNPs and the released Ag^+ ions in the growth medium. Silver nanoparticles and the released Ag^+ ions have caused reduction in the cell size. The typical length of an *E. coli* cell is about 2 μm, but in this research, cell length was reduced by half after exposure of the cells to AgNPs after 4 hours of treatment. Additionally, the shape of the cells changed, *E. coli* is a rod-shaped bacterium; however, AgNPs and the released Ag^+ ions caused reformation in the cell shape and altered it from bacilli to cocci. The changes in the cell size might be due to the stress of the presence of the released Ag^+ ions, and the cells decreased the exposed outer surface to survive

because cell size can affect the uptake of nutrients from outside of the cell (Miller et al., 2004). The released Ag^+ ions from the AgNPs can interrupt the signaling transduction in the cells, which might be the reason for the cells' loss of volume and change in morphology (Shrivastava et al., 2007). The antibacterial activity of silver nanoparticles affected *E. coli* H-NS protein and caused a spatial reorganization. The distribution of a major DNA-binding protein changed over the different incubation times in the presence of the released Ag^+ ions from AgNPs for 0H, 1H, 4H, 8H, and 12H. Despite the fact of having the cell size reduced to less than the size in the untreated medium, the H-NS proteins molecules formed large clusters concentrated mid-cell. Results shed light on a new affect caused by AgNPs and Ag^+ ions which has been neglected previously. The action mechanism of silver nanoparticles depends on the released silver ions (Zhang et al., 2016). Thus, Ag^+ ions might be playing an additional role in protein reorganization.

Chapter Four

4. Conclusion

This work is innovative because it is the first time to apply super-resolution fluorescence microscopy to examine the spatial reorganization of H-NS proteins in bacteria when subjected to AgNPs at the molecular level. The superior capability of super-resolution fluorescence microscopy allowed localization of individual H-NS proteins inside individual bacteria with great accuracy and precision. The spatial resolution of super-resolution achieved in our study is ~23 nm, which is about 10 times better than conventional fluorescence microscopy. In addition, the localizations of the H-NS proteins allowed performance of quantitative analysis on the spatial organization and changes in the organization, which were not accessible previously.

In this study, AgNPs and additional contribution of Ag^+ ions have caused morphological changes of *E. coli* bacteria. The lengths of the bacteria were shorter at 4 hours, 8 hours and 12 hours of treatment. More importantly, from the super-resolution fluorescence data, observation detected H-NS protein reorganization after treatment with AgNPs. In addition, algorithms based on Voronoi diagrams quantified the spatial organization of H-NS proteins. The occupied area by each H-NS molecule and the distance between neighboring H-NS molecules decreased which can explain the formation of dense and large clusters with the passage of the incubation duration from 0 to 12 hours in the presence of AgNPs. H-NS proteins molecular density distribution increased which can suggest an increase in DNA condensation. The H-NS proteins formed denser and larger clusters at the center of the bacteria after subjecting the bacteria to AgNPs and Ag^+ ions.

Based on the methodology of this research, it is expected to be readily applied to study the spatial reorganization of many biological molecules at the scale of nanometers caused by

AgNPs and Ag^+ ions, which will provide new prospective on the antimicrobial effect NPs on bacterial cell. For example, as H-NS is one of more than 12 nucleoid-associated proteins in bacteria, other nucleoid associated proteins are likely to be affected by AgNPs. Furthermore, a study by Ivask et al., 2014 examined more than 30 genes in terms of the toxicity of AgNPs and Ag^+ ions; the methodology employed in this research could be applied to those genes to investigate how AgNPs affect them. Also, due to the results of this research study, AgNPs with the released Ag^+ ions can be a major component in developing new antimicrobial materials to sterilize surfaces in medical treatment, such as medical equipment in operating rooms and other medical equipment that needs to be sterilized.

This research investigating H-NS proteins showed that AgNPs and the released Ag^+ ions caused denser and larger clusters at the center of the bacteria, which might lead to DNA condensation indirectly, as H-NS proteins are DNA binding proteins. Future studies can be done to investigate the state of DNA in the absence of H-NS proteins but in the presence of AgNPs. Furthermore, an *E. coli* strain with a deletion of the *hns* gene from the chromosome but supplemented with a plasmid carrying this gene was utilized. Although care was taken so that the expression level of H-NS proteins was not affected, repetition of the current study using a strain with H-NS-mEos3.2 fusion protein encoded directly in the bacterial chromosome, so that the strain is more like the wild type, is needed to confirm the results obtained in this study.

To summarize, antimicrobial activity and mechanisms of AgNPs and the released Ag^+ ions were investigated by examining the spatial organization of one major DNA binding protein – H-NS protein – using quantitative super-resolution fluorescence microscopy. Our work is important because it addresses the antibiotic resistance of bacteria, which has become one of the major global threats to public health. The current work provides new quantitative understanding

of the antimicrobial activity and mechanism of AgNPs, which is expected to help to develop new and more effective strategies to fight against resistant bacteria. In addition, due to the importance of H-NS proteins in bacteria, this study is expected to advance the understanding of how bacteria respond to external stimuli (in this specific study exposure to AgNPs).

References

Alexander, J. W. (2009). History of the Medical Use of Silver. *Surgical Infections*, *10*(3), 289–292. https://doi.org/10.1089/sur.2008.9941

Aminov, R. I. (2010). A Brief History of the Antibiotic Era: Lessons Learned and Challenges for the Future. *Frontiers in Microbiology*, *1*. https://doi.org/10.3389/fmicb.2010.00134

Ardani, H. K., Imawan, C., Handayani, W., Djuhana, D., Harmoko, A., & Fauzia, V. (2017). Enhancement of the stability of silver nanoparticles synthesized using aqueous extract of *Diospyros discolor* Willd. leaves using polyvinyl alcohol. *IOP Conference Series: Materials Science and Engineering*, *188*, 012056. https://doi.org/10.1088/1757-899X/188/1/012056

Baba, T., Ara, T., Hasegawa, M., Takai, Y., Okumura, Y., Baba, M., … Mori, H. (2006). Construction of Escherichia coli K-12 in-frame, single-gene knockout mutants: the Keio collection. *Molecular Systems Biology*, *2*. https://doi.org/10.1038/msb4100050

Badawy, A. M. E., Luxton, T. P., Silva, R. G., Scheckel, K. G., Suidan, M. T., & Tolaymat, T. M. (2010). Impact of Environmental Conditions (pH, Ionic Strength, and Electrolyte Type) on the Surface Charge and Aggregation of Silver Nanoparticles Suspensions. *Environmental Science & Technology*, *44*(4), 1260–1266. https://doi.org/10.1021/es902240k

Baker, C., Pradhan, A., Pakstis, L., Pochan, DarrinJ., & Shah, S. I. (2005). Synthesis and Antibacterial Properties of Silver Nanoparticles. *Journal of Nanoscience and Nanotechnology*, *5*(2), 244–249. https://doi.org/10.1166/jnn.2005.034

Balzarotti, F., Eilers, Y., Gwosch, K. C., Gynnå, A. H., Westphal, V., Stefani, F. D., … Hell, S. W. (2017). Nanometer resolution imaging and tracking of fluorescent molecules with minimal photon fluxes. *Science*, *355*(6325), 606–612. https://doi.org/10.1126/science.aak9913

Betzig, E., Patterson, G. H., Sougrat, R., Lindwasser, O. W., Olenych, S., Bonifacino, J. S., … Hess, H. F. (2006). Imaging Intracellular Fluorescent Proteins at Nanometer Resolution. *Science*, *313*(5793), 1642–1645. https://doi.org/10.1126/science.1127344

Bloch, V., Yang, Y., Margeat, E., Chavanieu, A., Augé, M. T., Robert, B., … Kochoyan, M. (2003). The H-NS dimerization domain defines a new fold contributing to DNA recognition. *Nature Structural & Molecular Biology*, *10*(3), 212–218. https://doi.org/10.1038/nsb904

Bradford, P. A. (2001). Extended-Spectrum -Lactamases in the 21st Century: Characterization, Epidemiology, and Detection of This Important Resistance Threat. *Clinical Microbiology Reviews*, *14*(4), 933–951. https://doi.org/10.1128/CMR.14.4.933-951.2001

Carlson, C., Hussain, S. M., Schrand, A. M., K. Braydich-Stolle, L., Hess, K. L., Jones, R. L., & Schlager, J. J. (2008). Unique Cellular Interaction of Silver Nanoparticles: Size-Dependent Generation of Reactive Oxygen Species. *The Journal of Physical Chemistry B*, *112*(43), 13608–13619. https://doi.org/10.1021/jp712087m

Chen, K. L., & Bothun, G. D. (2014). Nanoparticles Meet Cell Membranes: Probing Nonspecific Interactions using Model Membranes. *Environmental Science & Technology*, *48*(2), 873–880. https://doi.org/10.1021/es403864v

Chen, X., Zaro, J. L., & Shen, W.-C. (2013). Fusion protein linkers: Property, design and functionality. *Advanced Drug Delivery Reviews*, *65*(10), 1357–1369. https://doi.org/10.1016/j.addr.2012.09.039

Coltharp, C., Kessler, R. P., & Xiao, J. (2012). Accurate Construction of Photoactivated Localization Microscopy (PALM) Images for Quantitative Measurements. *PLoS ONE*, *7*(12), e51725. https://doi.org/10.1371/journal.pone.0051725

Dakal, T. C., Kumar, A., Majumdar, R. S., & Yadav, V. (2016). Mechanistic Basis of Antimicrobial Actions of Silver Nanoparticles. *Frontiers in Microbiology*, *7*. https://doi.org/10.3389/fmicb.2016.01831

Dame, R. T. (2000). H-NS mediated compaction of DNA visualised by atomic force microscopy. *Nucleic Acids Research*, *28*(18), 3504–3510. https://doi.org/10.1093/nar/28.18.3504

Danaei, M., Dehghankhold, M., Ataei, S., Hasanzadeh Davarani, F., Javanmard, R., Dokhani, A., … Mozafari, M. (2018). Impact of Particle Size and Polydispersity Index on the Clinical Applications of Lipidic Nanocarrier Systems. *Pharmaceutics*, *10*(2), 57. https://doi.org/10.3390/pharmaceutics10020057

Dorman, C. J. (2004). H-NS: a universal regulator for a dynamic genome. *Nature Reviews Microbiology*, *2*(5), 391–400. https://doi.org/10.1038/nrmicro883

Durisic, N., Laparra-Cuervo, L., Sandoval-Álvarez, Á., Borbely, J. S., & Lakadamyali, M. (2014). Single-molecule evaluation of fluorescent protein photoactivation efficiency using an in vivo nanotemplate. *Nature Methods*, *11*(2), 156–162. https://doi.org/10.1038/nmeth.2784

Escherich, T. (1988). *The Intestinal Bacteria of the Neonate and Breast-Fed Infant*. 7.

Ester, M., Kriegel, H.-P., & Xu, X. (1996). *A Density-Based Algorithm for Discovering Clusters in Large Spatial Databases with Noise*. 6.

Fair, R. J., & Tor, Y. (2014). Antibiotics and Bacterial Resistance in the 21st Century. *Perspectives in Medicinal Chemistry*, *6*, PMC.S14459. https://doi.org/10.4137/PMC.S14459

Feng, Q. L., Wu, J., Chen, G. Q., Cui, F. Z., Kim, T. N., & Kim, J. O. (2000). *A mechanistic study of the antibacterial effect of silver ions on Escherichia coli and Staphylococcus aureus*. 7.

Fissan, H., Ristig, S., Kaminski, H., Asbach, C., & Epple, M. (2014). Comparison of different characterization methods for nanoparticle dispersions before and after aerosolization. *Analytical Methods*, *6*(18), 7324. https://doi.org/10.1039/C4AY01203H

Fürstenberg, A., & Heilemann, M. (2013). Single-molecule localization microscopy – near-molecular spatial resolution in light microscopy with photoswitchable fluorophores. *Physical Chemistry Chemical Physics*, *15*(36), 14919. https://doi.org/10.1039/c3cp52289j

Gehrke, I., Geiser, A., & Somborn-Schulz, A. (2015). Innovations in nanotechnology for water treatment. *Nanotechnology, Science and Applications*, 1. https://doi.org/10.2147/NSA.S43773

Gong, P., Li, H., He, X., Wang, K., Hu, J., Tan, W., … Yang, X. (2007). Preparation and antibacterial activity of Fe_3O_4@Ag nanoparticles. *Nanotechnology*, *18*(28), 285604. https://doi.org/10.1088/0957-4484/18/28/285604

Gould, I. M., & Bal, A. M. (2013). New antibiotic agents in the pipeline and how they can help overcome microbial resistance. *Virulence*, *4*(2), 185–191. https://doi.org/10.4161/viru.22507

Haider, M. J., & Mehdi, M. S. (2014). *Study of morphology and Zeta Potential analyzer for the Silver Nanoparticles*. *5*(7), 7.

Haque, M. A., Imamura, R., Brown, G. A., Krishnamurthi, V. R., Niyonshuti, I. I., Marcelle, T., … Wang, Y. (2017a). An experiment-based model quantifying antimicrobial activity of silver nanoparticles on *Escherichia coli*. *RSC Advances*, *7*(89), 56173–56182. https://doi.org/10.1039/C7RA10495B

Haque, M. A., Imamura, R., Brown, G. A., Krishnamurthi, V. R., Niyonshuti, I. I., Marcelle, T., … Wang, Y. (2017b). An experiment-based model quantifying antimicrobial activity of silver nanoparticles on *Escherichia coli*. *RSC Advances*, *7*(89), 56173–56182. https://doi.org/10.1039/C7RA10495B

Hassani, H., & Silva, E. (2015). A Kolmogorov-Smirnov Based Test for Comparing the Predictive Accuracy of Two Sets of Forecasts. *Econometrics*, *3*(3), 590–609. https://doi.org/10.3390/econometrics3030590

Hess, S. T., Girirajan, T. P. K., & Mason, M. D. (2006). Ultra-High Resolution Imaging by Fluorescence Photoactivation Localization Microscopy. *Biophysical Journal*, *91*(11), 4258–4272. https://doi.org/10.1529/biophysj.106.091116

Hipler, U.-C., & Elsner, P. (Eds.). (2006). *Biofunctional textiles and the skin*. Basel ; New York: Karger.

Hommais, F., Krin, E., Laurent-Winter, C., Soutourina, O., Malpertuy, A., Le Caer, J.-P., … Bertin, P. (2001). Large-scale monitoring of pleiotropic regulation of gene expression by the prokaryotic nucleoid-associated protein, H-NS: Global control of gene expression by H-NS. *Molecular Microbiology*, *40*(1), 20–36. https://doi.org/10.1046/j.1365-2958.2001.02358.x

Huang, B., Babcock, H., & Zhuang, X. (2010). Breaking the Diffraction Barrier: Super-Resolution Imaging of Cells. *Cell*, *143*(7), 1047–1058. https://doi.org/10.1016/j.cell.2010.12.002

Huang, B., Bates, M., & Zhuang, X. (2009). Super-Resolution Fluorescence Microscopy. *Annual Review of Biochemistry*, *78*(1), 993–1016. https://doi.org/10.1146/annurev.biochem.77.061906.092014

In, J., & Lee, S. (2017). Statistical data presentation. *Korean Journal of Anesthesiology*, *70*(3), 267. https://doi.org/10.4097/kjae.2017.70.3.267

Infectious Diseases Society of America (IDSA). (2011). Combating Antimicrobial Resistance: Policy Recommendations to Save Lives. *Clinical Infectious Diseases*, *52*(suppl_5), S397–S428. https://doi.org/10.1093/cid/cir153

Instruments, M. (2011). *Dynamic light scattering common terms defined*. 6.

Jiang, S., Park, S., Challapalli, S. D., Fei, J., & Wang, Y. (2017). Robust nonparametric quantification of clustering density of molecules in single-molecule localization microscopy. *PLOS ONE*, *12*(6), e0179975. https://doi.org/10.1371/journal.pone.0179975

Jung, W. K., Koo, H. C., Kim, K. W., Shin, S., Kim, S. H., & Park, Y. H. (2008). Antibacterial Activity and Mechanism of Action of the Silver Ion in Staphylococcus aureus and Escherichia coli. *Applied and Environmental Microbiology*, *74*(7), 2171–2178. https://doi.org/10.1128/AEM.02001-07

Kędziora, A., Speruda, M., Krzyżewska, E., Rybka, J., Łukowiak, A., & Bugla-Płoskońska, G. (2018). Similarities and Differences between Silver Ions and Silver in Nanoforms as Antibacterial Agents. *International Journal of Molecular Sciences*, *19*(2), 444. https://doi.org/10.3390/ijms19020444

Kreuter, J. (2007). Nanoparticles—a historical perspective. *International Journal of Pharmaceutics*, *331*(1), 1–10. https://doi.org/10.1016/j.ijpharm.2006.10.021

Kuhnert, P., Nicolet, J., & Frey, J. (1995). *Rapid and Accurate Identification of Escherichia coli K-12 Strains*. *61*, 5.

Levet, F., Hosy, E., Kechkar, A., Butler, C., Beghin, A., Choquet, D., & Sibarita, J.-B. (2015). SR-Tesseler: a method to segment and quantify localization-based super-resolution microscopy data. *Nature Methods*, *12*(11), 1065–1071. https://doi.org/10.1038/nmeth.3579

Lin, P.-C., Lin, S., Wang, P. C., & Sridhar, R. (2014). Techniques for physicochemical characterization of nanomaterials. *Biotechnology Advances*, *32*(4), 711–726. https://doi.org/10.1016/j.biotechadv.2013.11.006

Liu, S., Wei, L., Hao, L., Fang, N., Chang, M. W., Xu, R., … Chen, Y. (2009). Sharper and Faster "Nano Darts" Kill More Bacteria: A Study of Antibacterial Activity of Individually Dispersed Pristine Single-Walled Carbon Nanotube. *ACS Nano*, *3*(12), 3891–3902. https://doi.org/10.1021/nn901252r

Liu, Y. (2008). Box plots: use and interpretation. *Transfusion*, *48*(11), 2279–2280. https://doi.org/10.1111/j.1537-2995.2008.01925.x

Lok, C.-N., Ho, C.-M., Chen, R., He, Q.-Y., Yu, W.-Y., Sun, H., … Che, C.-M. (2006). Proteomic Analysis of the Mode of Antibacterial Action of Silver Nanoparticles. *Journal of Proteome Research*, *5*(4), 916–924. https://doi.org/10.1021/pr0504079

Long, Y.-M., Hu, L.-G., Yan, X.-T., Zhao, X.-C., Zhou, Q.-F., Cai, Y., & Jiang, G.-B. (2017). Surface ligand controls silver ion release of nanosilver and its antibacterial activity against Escherichia coli. *International Journal of Nanomedicine*, *Volume 12*, 3193–3206. https://doi.org/10.2147/IJN.S132327

Loo, C., Lowery, A., Halas, N., West, J., & Drezek, R. (2005). Immunotargeted Nanoshells for Integrated Cancer Imaging and Therapy. *Nano Letters*, *5*(4), 709–711. https://doi.org/10.1021/nl050127s

M9, Minimal Salts, 5X M6030. (n.d.). Retrieved February 8, 2019, from Sigma-Aldrich website: https://www.sigmaaldrich.com/catalog/product/sigma/m6030

McKinney, S. A., Murphy, C. S., Hazelwood, K. L., & Looger, L. L. (2009). *A bright and photostable photoconvertible fluorescent protein for fusion tags*. 9.

McShan, D., Ray, P. C., & Yu, H. (2014). Molecular toxicity mechanism of nanosilver. *Journal of Food and Drug Analysis*, *22*(1), 116–127. https://doi.org/10.1016/j.jfda.2014.01.010

Miller, C., Thomsen, L. E., Gaggero, C., Mosseri, R., Ingmer, H., & Cohen, S. N. (2004). *Against Antibiotic Lethality*. *305*, 4.

Morones, J. R., Elechiguerra, J. L., Camacho, A., Holt, K., Kouri, J. B., Ramírez, J. T., & Yacaman, M. J. (2005). The bactericidal effect of silver nanoparticles. *Nanotechnology*, *16*(10), 2346–2353. https://doi.org/10.1088/0957-4484/16/10/059

nanoComposix, nanoComposix. (2012). *NANOCOMPOSIX'S GUIDE TO DYNAMIC LIGHT SCATTERING MEASUREMENT AND ANALYSIS*. *1.3*. Retrieved from https://www.researchgate.net/profile/Faris_Alshubiri/...DLS.../5003.pdf

Navarre, W. W., Porwollik, S., Wang, Y., McClelland, M., Rosen, H., Libby, S. J., & Fang, F. C. (2006). Selective Silencing of Foreign DNA with Low GC Content by the H-NS Protein in Salmonella. *Science, New Series*, *313*(5784), 236–238.

Pal, S., Tak, Y. K., & Song, J. M. (2007). Does the Antibacterial Activity of Silver Nanoparticles Depend on the Shape of the Nanoparticle? A Study of the Gram-Negative Bacterium Escherichia coli. *Applied and Environmental Microbiology*, *73*(6), 1712–1720. https://doi.org/10.1128/AEM.02218-06

Phanjom, P., & Ahmed, G. (2017). Effect of different physicochemical conditions on the synthesis of silver nanoparticles using fungal cell filtrate of *Aspergillus oryzae* (MTCC No. 1846) and their antibacterial effect. *Advances in Natural Sciences: Nanoscience and Nanotechnology*, *8*(4), 045016. https://doi.org/10.1088/2043-6254/aa92bc

Powers, K. W., Brown, S. C., Krishna, V. B., Wasdo, S. C., Moudgil, B. M., & Roberts, S. M. (2006). Research Strategies for Safety Evaluation of Nanomaterials. Part VI. Characterization of Nanoscale Particles for Toxicological Evaluation. *Toxicological Sciences*, *90*(2), 296–303. https://doi.org/10.1093/toxsci/kfj099

Rai, M. K., Deshmukh, S. D., Ingle, A. P., & Gade, A. K. (2012). Silver nanoparticles: the powerful nanoweapon against multidrug-resistant bacteria: Activity of silver nanoparticles against MDR bacteria. *Journal of Applied Microbiology*, *112*(5), 841–852. https://doi.org/10.1111/j.1365-2672.2012.05253.x

Rai, M., Yadav, A., & Gade, A. (2009). Silver nanoparticles as a new generation of antimicrobials. *Biotechnology Advances*, *27*(1), 76–83. https://doi.org/10.1016/j.biotechadv.2008.09.002

Rayamajhi, N., Cha, S. B., & Yoo, H. S. (2010). *Antibiotics Resistances: Past, Present and Future*. 17.

Rust, M. J., Bates, M., & Zhuang, X. (2006). Sub-diffraction-limit imaging by stochastic optical reconstruction microscopy (STORM). *Nature Methods*, *3*(10), 793–796. https://doi.org/10.1038/nmeth929

Sastry, M., Patil, V., & Sainkar, S. R. (1998). Electrostatically Controlled Diffusion of Carboxylic Acid Derivatized Silver Colloidal Particles in Thermally Evaporated Fatty Amine Films. *The Journal of Physical Chemistry B*, *102*(8), 1404–1410. https://doi.org/10.1021/jp9719873

Schindelin, J., Arganda-Carreras, I., Frise, E., Kaynig, V., Longair, M., Pietzsch, T., … Cardona, A. (2012). Fiji: an open-source platform for biological-image analysis. *Nature Methods*, *9*(7), 676–682. https://doi.org/10.1038/nmeth.2019

Schmidt, H. (2017). *Exposure to Silver Nanoparticles Affects Biofilm Structure and Adhesiveness*. *1*(2), 9.

Sengupta, P., & Lippincott-Schwartz, J. (2012). Quantitative analysis of photoactivated localization microscopy (PALM) datasets using pair-correlation analysis. *BioEssays*, *34*(5), 396–405. https://doi.org/10.1002/bies.201200022

Sharma, G., Sharma, A. R., Kurian, M., Bhavesh, R., Nam, J. S., & Lee, S. S. (2014). *GREEN SYNTHESIS OF SILVER NANOPARTICLE USING MYRISTICA FRAGRANS (NUTMEG) SEED EXTRACT AND ITS BIOLOGICAL ACTIVITY*. 8.

Shrivastava, S., Bera, T., Roy, A., Singh, G., Ramachandrarao, P., & Dash, D. (2007). Characterization of enhanced antibacterial effects of novel silver nanoparticles. *Nanotechnology*, *18*(22), 225103. https://doi.org/10.1088/0957-4484/18/22/225103

Silver, S., Phung, L. T., & Silver, G. (2006). Silver as biocides in burn and wound dressings and bacterial resistance to silver compounds. *Journal of Industrial Microbiology & Biotechnology*, *33*(7), 627–634. https://doi.org/10.1007/s10295-006-0139-7

Singh, K., Milstein, J. N., & Navarre, W. W. (2016). Xenogeneic Silencing and Its Impact on Bacterial Genomes. *Annual Review of Microbiology*, *70*(1), 199–213. https://doi.org/10.1146/annurev-micro-102215-095301

Stuurman, N., Edelstein, A. D., Amodaj, N., Hoover, K. H., & Vale, R. D. (2010). Computer Control of Microscopes using μManager. *Current Protocols in Molecular Biology / Edited by Frederick M. Ausubel ... [et Al.]*, *CHAPTER*, Unit14.20. https://doi.org/10.1002/0471142727.mb1420s92

Tan, S., & Tatsumura, Y. (2015). Alexander Fleming (1881–1955): Discoverer of penicillin. *Singapore Medical Journal*, *56*(07), 366–367. https://doi.org/10.11622/smedj.2015105

Tenaillon, O., Skurnik, D., Picard, B., & Denamur, E. (2010). The population genetics of commensal Escherichia coli. *Nature Reviews Microbiology*, *8*(3), 207–217. https://doi.org/10.1038/nrmicro2298

Thorley, A. J., & Tetley, T. D. (2013). New perspectives in nanomedicine. *Pharmacology & Therapeutics*, *140*(2), 176–185. https://doi.org/10.1016/j.pharmthera.2013.06.008

Thorley, J. A., Pike, J., & Rappoport, J. Z. (2014). Super-resolution Microscopy. In *Fluorescence Microscopy* (pp. 199–212). https://doi.org/10.1016/B978-0-12-409513-7.00014-2

Tu, W., Fang, Z., Li, Q., Shaw, S.-L., & Chen, B. (2014). A bi-level Voronoi diagram-based metaheuristic for a large-scale multi-depot vehicle routing problem. *Transportation Research Part E: Logistics and Transportation Review*, *61*, 84–97. https://doi.org/10.1016/j.tre.2013.11.003

Tupper, A. E., Owen-Hughes, T. A., Ussery, D. W., Santos, D. S., Ferguson, D. J. P., Sidebotham, J. M., … Higgins, C. F. (1994). *The chromatin-associated protein H-NS alters DNA topology in vitro*. 11.

Ventola, C. L. (2015). *The Antibiotic Resistance Crisis*. 7.

Wang, W., Li, G.-W., Chen, C., Xie, X. S., & Zhuang, X. (2011). Chromosome Organization by a Nucleoid-Associated Protein in Live Bacteria. *Science*, *333*(6048), 1445–1449. https://doi.org/10.1126/science.1204697

Wang, X.-J., Du, G.-J., Zhao, S.-Q., Yan, M., & Gu, L.-Q. (2009). Synthesis and Antibacterial Activity of a Series of α-Substituted Acetylpiperazinyl Oxazolidinones. *Chemical Biology & Drug Design*, *74*(3), 276–281. https://doi.org/10.1111/j.1747-0285.2009.00859.x

Wang, Yi, Zheng, Y., Huang, C. Z., & Xia, Y. (2013). Synthesis of Ag Nanocubes 18–32 nm in Edge Length: The Effects of Polyol on Reduction Kinetics, Size Control, and Reproducibility. *Journal of the American Chemical Society*, *135*(5), 1941–1951. https://doi.org/10.1021/ja311503q

Wang, Yina, Schnitzbauer, J., Hu, Z., Li, X., Cheng, Y., Huang, Z.-L., & Huang, B. (2014). Localization events-based sample drift correction for localization microscopy with redundant cross-correlation algorithm. *Optics Express*, *22*(13), 15982. https://doi.org/10.1364/OE.22.015982

Wang, Yong, Penkul, P., & Milstein, J. N. (2016). Quantitative Localization Microscopy Reveals a Novel Organization of a High-Copy Number Plasmid. *Biophysical Journal*, *111*(3), 467–479. https://doi.org/10.1016/j.bpj.2016.06.033

Welz, B. (1999). Atomic absorption spectrometry ☤ pregnant again after 45 years. *Atomic Spectroscopy*, 14.

Wolter, S., Löschberger, A., Holm, T., Aufmkolk, S., Dabauvalle, M.-C., van de Linde, S., & Sauer, M. (2012a). rapidSTORM: accurate, fast open-source software for localization microscopy. *Nature Methods*, *9*(11), 1040–1041. https://doi.org/10.1038/nmeth.2224

Wolter, S., Löschberger, A., Holm, T., Aufmkolk, S., Dabauvalle, M.-C., van de Linde, S., & Sauer, M. (2012b). rapidSTORM: accurate, fast open-source software for localization microscopy. *Nature Methods*, *9*(11), 1040–1041. https://doi.org/10.1038/nmeth.2224

Zhang, M., Chang, H., Zhang, Y., Yu, J., Wu, L., Ji, W., … Xu, T. (2012). Rational design of true monomeric and bright photoactivatable fluorescent proteins. *Nature Methods*, *9*(7), 727–729. https://doi.org/10.1038/nmeth.2021

Zhang, X.-F., Liu, Z.-G., Shen, W., & Gurunathan, S. (2016). Silver Nanoparticles: Synthesis, Characterization, Properties, Applications, and Therapeutic Approaches. *International Journal of Molecular Sciences*, *17*(9), 1534. https://doi.org/10.3390/ijms17091534

Zhang, Y., Yang, M., Portney, N. G., Cui, D., Budak, G., Ozbay, E., … Ozkan, C. S. (2008). Zeta potential: a surface electrical characteristic to probe the interaction of nanoparticles with normal and cancer human breast epithelial cells. *Biomedical Microdevices*, *10*(2), 321–328. https://doi.org/10.1007/s10544-007-9139-2